

Unbiased analysis of primordial non-Gaussianity: the multipoles of the full relativistic power spectrum

Chris Addis,^{a,1} Sêcloka L. Guedezounme,^b Jessie Hammond,^a Chris Clarkson,^{a,b} Federico Montano,^{c,d} Stefano Camera,^{c,d,e,b} Sheean Jolicoeur,^{f,b} and Roy Maartens^{b,h}

^aAstronomy Unit, School of Physical & Chemical Sciences, Queen Mary University of London, London E1 4NS, UK

^bDepartment of Physics & Astronomy, University of Western Cape, Cape Town 7535, South Africa

^cDipartimento di Fisica, Università degli Studi di Torino, Via P. Giuria 1, 10125 Torino, Italy

^dINFN – Istituto Nazionale di Fisica Nucleare, Sezione di Torino, Via P. Giuria 1, 10125 Torino, Italy

^eINAF – Istituto Nazionale di Astrofisica, Osservatorio Astrofisico di Torino, Strada Osservatorio 20, 10025 Pino Torinese, Italy

^fVIT Mauritius, Unicity International Education Hub, 72448, Pierrefonds, Mauritius

^hNational Institute for Theoretical & Computational Sciences, Cape Town 7535, South Africa
E-mail: c.l.j.addis@qmul.ac.uk, seclokaguedezounme@gmail.com,

j.r.hammond@qmul.ac.uk, chris.clarkson@qmul.ac.uk, federico.montano@unito.it,
stefano.camera@unito.it, jolicoeurnsheean@gmail.com, roy.maartens@gmail.com

Abstract. A major goal of ongoing and future cosmological surveys of the large-scale structure is to measure local type primordial non-Gaussianity in the galaxy power spectrum through the scale-dependent bias. General relativistic effects have been shown to be degenerate with this measurement and therefore one needs to consider a non-Newtonian approach. In this work, we develop a consistent framework to compute integrated effects, including lensing convergence, time delay, and integrated Sachs–Wolfe, along with the local relativistic projection and wide-separation corrections in the multipoles of the power spectrum. We show that, for a *Euclid*-like H α -line galaxy survey and a MegaMapper-like Lyman-break galaxy survey, ignoring these effects leads to a bias on the best fit measurement of the amplitude of primordial non-Gaussianity, f_{NL} , of around 3σ and 20σ respectively. When we include these corrections, the uncertainty in our knowledge of the luminosity function leads to further uncertainty in our measurement of f_{NL} . However, we show that this degeneracy can be partly mitigated by using a bright-faint multi-tracer analysis, where the observed galaxy sample is subdivided into two separate populations based on luminosity. This provides a 15–20% improvement on the forecasted constraints of local type f_{NL} . In addition, we present a novel calculation of the full multi-tracer covariance with the inclusion of wide-separation corrections. All of these results are implemented in the *Python* code COSMOWAP.

¹Corresponding author.

Contents

1	Introduction	2
2	Local Power Spectrum	4
2.1	Galaxy Number Counts and the Local Two-Point Function	5
2.2	Integrated Contributions to the Local Power Spectrum	7
2.2.1	LOS Dependence of the Local Power Spectrum	8
2.3	Survey Power Spectrum Multipoles	9
3	Forecast Setup	9
4	Results and Discussion	13
4.1	Integrated Contributions to the Power Spectrum	13
4.1.1	Non-linear Contributions to the Integrated Effects	14
4.2	Bias on Inference of PNG	15
4.3	Constraints on Local PNG	18
4.3.1	Multi-Tracer Analysis	22
5	Summary and Conclusions	22
A	Survey Details	24
A.1	Bright-Faint Split	25
B	Cross-Multipole Multi-Tracer Covariance	26
B.1	Covariance Matrix Element	26
B.1.1	Plane-parallel Constant Redshift Limit	27
B.1.2	Wide-Separation Corrections to the Covariance	28
B.2	Integrated Contributions to the Covariance	33
C	Integrated \times Local Contribution to the Local Power Spectrum	33
D	Local Kernels	34
E	Bias from Non-linear Contributions to the Integrated Effects	35
F	LOS Dependence of the Local Power Spectrum	35
F.1	Mixing in the Integrated terms beyond the Limber approximation	36
G	Properties of the Integrands	38
G.1	Convergence and Divergence and Computation Time	40
H	ISW, Time Delay and Lensing Contributions	41
I	Additional Plots	42

1 Introduction

Over the past few decades, there have been rapid experimental advances in our surveys of the large-scale structure of the universe. The next generation of spectroscopic galaxy surveys such as the ongoing Dark Energy Spectroscopic Instrument (DESI) [1] and *Euclid* [2] surveys as well as the future planned missions of SPHEREx [3], Nancy Grace Roman Space Telescope (WFIRST) [4] and MegaMapper [5] will go a step further, providing an even higher number density of detected objects over larger volumes and redshift ranges [see, for example, Figure 1 of 6]. With this increased statistical power, it becomes critical to fully consider previously subdominant theoretical systematics.

A major goal for these surveys is to constrain Primordial non-Gaussianity (PNG), which can provide insight on the physics of the early universe [7]. Currently, the tightest constraints on local PNG, determined via the parameter f_{NL} , come from observations of the cosmic microwave background (CMB) by *Planck* [8] who found $f_{NL} = 0.9 \pm 5.1$. Handily, local type PNG leaves an imprint in large-scale structure (LSS) not just in higher-order statistics, such as the bispectrum, but also in the power spectrum through the scale-dependent halo bias [9–11]. Next-generation galaxy surveys should provide competitive constraints with $\mathcal{O}(1)$ uncertainties using these observables [12–15].

Observations of LSS on our past light-cone are subject to distortions along our line-of-sight (LOS); to account for this projection along our LOS, the standard Newtonian ‘Kaiser’ [16, 17] treatment of redshift space distortions (RSD), which takes into account the main contribution from the peculiar velocity of the source, has usually been sufficient. However, with next-generation surveys probing larger scales and with increased precision this simplified analysis could lead to biased conclusions. Linear relativistic corrections to galaxy number counts such as the relativistic Doppler and gravitational redshift corrections have been known for some time [18–21]. As they are generally more prevalent on large scales, they have been shown to be degenerate with the local f_{NL} signal both in the angular [22–26] and the 3D Fourier [27–31] power spectrum and can lead to biases in our constraints on f_{NL} for future surveys at $\mathcal{O}(1)$ if they are neglected. More recent analyses [28, 31] have also accounted for the sensitivity of these effects to the luminosity threshold for the survey through evolution, b_e , and magnification, Q , biases (see 32 for an overview). The uncertainty in our knowledge of the luminosity function for a given survey therefore leads to greater uncertainty in the measurement of f_{NL} .

Alternatively, detecting these relativistic projection effects themselves has attracted interest, as they are sensitive to the metric potentials, Φ and Ψ , in a different way to the Kaiser terms and, as such, can be used to construct tests of general relativity [33–37]. When detecting these effects, it is advantageous to use the multipoles of the 3D power spectrum (or 2-point correlation function, 2-PCF) rather than the angular equivalent, as not only does it allow us to access information from the full 3D spectroscopic map, but one can also isolate the leading order relativistic contribution in the odd-parity multipoles in a multi-tracer analysis [e.g. 18, 38]. Within the bright-faint split approach, as proposed by [39–41], a single galaxy population is split according to luminosity into two independent populations, which can lead to improved constraining power on relativistic effects in the multi-tracer power spectrum [40–44]. Since working with the multipoles of the Fourier power spectrum is also common for PNG analysis, developing a consistent framework to include these relativistic effects is essential.

Multi-tracer techniques have also been proposed to improve observational constraints on f_{NL} by using highly biased samples [45–47], as for two tracers, A and B, the constraining

power, in the cosmic variance limit, is $\propto |b_1^B b_\phi^A - b_1^A b_\phi^B|$ (or just $\propto |b_1^A - b_1^B|$ under the universality relation [10]). Therefore, this motivates developing a fully relativistic multi-tracer framework whereby we can use highly biased tracers to not only maximise the f_{NL} signal but also to better constrain our uncertainties in the luminosity function.

While integrated corrections (lensing convergence, time delay, and integrated Sachs-Wolfe, ISW) to the galaxy number counts have been commonly included in angular analyses, their inclusion in the Fourier power spectrum is less straightforward. Our goal in this paper is to consistently include these contributions in a $P(k)$ analysis of f_{NL} . One approach is to derive them starting from the 2-PCF, [29, 48, 49] but this can be cumbersome and numerically expensive. The exact nature of these integrated effects in the 3D power spectrum, which, beyond the Limber approximation [50], break local translation invariance in our local 2-point function is subtle, and has not yet been fully explored. Therefore, we adopt and expand upon the formalism presented in [51], where integrated effects can be directly computed in the Cartesian Fourier space, to allow for integrated effects to be correctly modelled at wide-separations. Further, we extend this framework to include integrated cross integrated, ($I \times I$), contributions to the power spectrum multipoles.

The multipoles of the power spectrum can be measured from a given survey using the efficient and simple ‘Yamamoto’ estimator [52–55]. However, in order to compute this quantity theoretically it is convenient to define the ‘local’ 2-point function/power spectrum, which is defined for a single LOS and therefore, one can define the local multipoles [17, 55–58]¹. To include the full LOS information in this local region, where we are correlating a pair of points, one then typically relies on a perturbative expansion [19, 51, 59, 60]. These corrections contain the part of the signal which breaks translation invariance in our local statistic and as such become relevant when considering large pair separations; therefore they are termed wide-separation corrections (WS). Here, the term wide-separation describes the corrections deriving from this symmetry breaking both angularly, due to RSD (termed wide-angle corrections), and radially, due to evolution (termed radial evolution corrections). As they arise on large scales, these corrections are degenerate with signals of local PNG and relativistic effects [30, 31, 51, 60, 61] and therefore must be considered for a consistent analysis on large scales. Indeed, with Stage-IV surveys, all of these corrections become relevant not only due to the increased precision, but also as these surveys map increased volume, we gain access to ultra-large-scale modes.

At very large separations and low redshifts, this perturbative wide-separation expansion breaks down [e.g. 62], and an alternative basis, such as spherical Fourier-Bessel (sFB), is more appropriate; see [63, 64] for recent work including relativistic effects in the sFB formalism. However, for the majority of ongoing and upcoming galaxy surveys, the power spectrum multipoles remain a practical basis for analysis.

This work therefore attempts to provide a consistent framework for computing these light-cone effects (including all relevant relativistic and wide-separation effects) in the multipoles of the Fourier power spectrum and we are explicit in how this is connected to observable quantities (cf. Section 2). In particular, we focus on the integrated contributions and their contribution to the local power spectrum (Section 2.2), and then construct forecasts (Section

¹One can also consider this as: without translation invariance, the Fourier modes are no longer statistically independent. The position-dependent line-of-sight induces geometric mode-mode coupling. Consequently, the power spectrum is no longer the Fourier conjugate of the two-point correlation function, and the field’s statistical properties are spread into off-diagonal terms of the covariance matrix rather than being contained solely in the diagonal.

[3](#)), on the impact of these effects on PNG for these effects for a few different survey setups (Section [A](#)). We show that neglecting these effects can lead to a bias on the inference of local f_{NL} and that when including these effects, the uncertainty of our luminosity function leads to a greater uncertainty in our determination of f_{NL} . We also show how constraints on f_{NL} can then be improved with a multi-tracer approach by better constraining our evolution and magnification bias. We present a novel calculation of the analytic multi-tracer power spectrum multipole covariance on large-scales, with the inclusion of wide-separation corrections for the first time, Section [B](#). All of these results, including forecast code, is included in the *Python* code COSMOWAP [58, 65] with companion *Mathematica* notebooks included in MATHWAP [66].

2 Local Power Spectrum

Throughout this work, we adopt the following Fourier notation

$$\int_{\mathbf{x}_{12}} = \int d^3x_{12} \text{ and } \int_{\mathbf{k}} = \int \frac{d^3k}{(2\pi)^3}, \quad (2.1)$$

such that we can define our Fourier and inverse Fourier transforms, respectively as

$$F(\mathbf{k}) = \int_{\mathbf{x}} e^{-i\mathbf{k}\cdot\mathbf{x}} f(\mathbf{x}) \text{ and } f(\mathbf{x}) = \int_{\mathbf{k}} e^{i\mathbf{k}\cdot\mathbf{x}} F(\mathbf{k}). \quad (2.2)$$

We also refer to ‘local’ (non-integrated) contributions, e.g. Kaiser and local relativistic terms, and ‘local’ power spectrum - the region in which we do our wide-separation expansion.

Starting from the Yamamoto estimator [52, 53] for the multipoles of the power spectrum

$$\hat{P}_\ell^{ab}(k) = \frac{2\ell+1}{N_k} \int_{\mathcal{S}_1} d^3q_1 \int_{\mathcal{S}_2} d^3q_2 \delta_D(\mathbf{q}_1 + \mathbf{q}_2) \int_{\mathbf{x}_1, \mathbf{x}_2} e^{-i(\mathbf{q}_1 \cdot \mathbf{x}_1 + \mathbf{q}_2 \cdot \mathbf{x}_2)} \Delta_W^a(\mathbf{x}_1) \Delta_W^b(\mathbf{x}_2) \mathcal{L}_\ell(\hat{\mathbf{q}}_1 \cdot \hat{\mathbf{d}}), \quad (2.3)$$

where our LOS, \mathbf{d} , is varying across the survey but is set to an ‘endpoint’ LOS (either \mathbf{x}_1 or \mathbf{x}_2), for each local 2-point function region, such that the integrals in the estimator become separable and therefore computable with Fast Fourier Transforms (FFTs) [54, 55]. Here, $\Delta_W(\mathbf{x}) = \Delta(\mathbf{x}) W(\mathbf{x})$ represents the windowed field for a given survey window function, $W(\mathbf{x})$. The Fourier integrals represent discrete sums, $\int_{\mathcal{S}_i} d^3q_i F(\mathbf{q}_i) \equiv \sum_{\mathcal{S}_i} F(\mathbf{q}_i)$, over thin k -space shells, \mathcal{S}_i , of width Δk , centred at k_i , such that $\mathcal{S}_i \equiv \mathcal{S}(k_i | \Delta k)$ is the region of k -magnitudes contained by a given k_i -bin, $k_i - \Delta k/2 \leq k < k_i + \Delta k/2$. Finally, N_k represents the number of k -modes in each bin,

$$N_k = k_f^{-3} \int_{\mathcal{S}_1} d^3q_1 \int_{\mathcal{S}_2} d^3q_2 \delta_D(\mathbf{q}_1 + \mathbf{q}_2), \quad (2.4)$$

where k_f is the fundamental frequency of the survey box and N_k simplifies to $4\pi k^2 \Delta k / k_f^3$ in the continuous limit. For $\ell = 0$, this then reduces to the FKP estimator [67]. If we consider the unwindowed ‘true’ theory², then as shown in [55], this estimator can be related to the definition of the ‘local’ power spectrum.

²This significantly simplifies our forecasts but we note, we could include the impact of the convolution with the survey window in the standard way; whereby, one can use Hankel transforms to include the survey window function multiplicatively in the 2-point function, which can then be related to the windowed multipoles of the power spectrum using another Hankel transform [68].

Using the change of variables

$$\int d^3\mathbf{x}_1 \int d^3\mathbf{x}_2 \rightarrow \int d^3\mathbf{d} \int d^3\mathbf{x}_{12} \quad (2.5)$$

where $\mathbf{x}_{12} = \mathbf{x}_1 - \mathbf{x}_2$, and splitting the integration in each shell

$$\int_{S_i} d^3\mathbf{q}_i = \int_{k_i - \Delta k/2}^{k_i + \Delta k/2} dq_i q_i^2 \int d\Omega_{q_i}, \quad (2.6)$$

where $d\Omega_q$ is the infinitesimal solid angle, the corresponding theoretical multipoles can be expressed in the familiar form:

$$\hat{P}_\ell^{ab}(k) = (2\ell + 1) \int \frac{d\Omega_k}{4\pi} \int d^3\mathbf{d} \left[P_{\text{loc}}^{ab}(k, \mu; d) \mathcal{L}(\mu) \right], \quad (2.7)$$

where $\mu = \hat{\mathbf{k}} \cdot \hat{\mathbf{d}}$ specifies the LOS orientation of the k -vector, and we define the local power spectrum

$$P_{\text{loc}}^{ab}(k, \mu; d) = \int_{\mathbf{x}_{12}} e^{-i\mathbf{k}\cdot\mathbf{x}_{12}} \langle \Delta^a(\mathbf{x}_1) \Delta^b(\mathbf{x}_2) \rangle, \quad (2.8)$$

which is defined at a single position, \mathbf{d} . This is then the Fourier transform of our ‘local’ 2-point function $\langle \Delta(\mathbf{x}_1) \Delta(\mathbf{x}_2) \rangle \equiv \xi_{\text{loc}}(\mathbf{x}_1, \mathbf{x}_2) \equiv \xi_{\text{loc}}(\mathbf{x}_{12}, \mathbf{d})$ which is simply ensemble average of our 2-point function over our local region; the common key assumption that makes the local power spectrum an easily computable quantity, is translation invariance, such that the statistics of the underlying dark matter density field at \mathbf{x}_1 and \mathbf{x}_2 are the same³. However, with large separations and integrated contributions computing the full local power spectrum that corresponds to the estimator is more subtle and we discuss this in the next section.

2.1 Galaxy Number Counts and the Local Two-Point Function

The number of galaxies in a given survey volume can be expressed in terms of standard terms ‘S’ – linear bias plus linear ‘Newtonian’ RSD, which we describe as the Kaiser term –, the non-integrated (local/source) relativistic projection ‘NI’, and integrated ‘I’ contributions

$$\Delta(\mathbf{x}) = \Delta^S(\mathbf{x}) + \Delta^{\text{NI}}(\mathbf{x}) + \Delta^I(\mathbf{x}). \quad (2.9)$$

These position space quantities can then be defined from the simple Fourier space kernels,

$$\Delta(\mathbf{x}) = \int_{\mathbf{q}} [\mathcal{K}^S(\mathbf{q}, \mathbf{x}) + \mathcal{K}^{\text{NI}}(\mathbf{q}, \mathbf{x})] \delta_0(\mathbf{q}) + \int_0^x dr \int_{\mathbf{q}} e^{i\mathbf{q}\cdot\mathbf{r}} \mathcal{K}^I(\mathbf{q}, \mathbf{x}, \mathbf{r}) \delta_0(\mathbf{q}), \quad (2.10)$$

where δ_0 is the linear matter overdensity, $\mathcal{K}^S(\mathbf{q}, \mathbf{x})$ is the standard RSD Kaiser kernel [16], $\mathcal{K}^{\text{NI}}(\mathbf{q}, \mathbf{x})$, is the linear local relativistic projection kernel [19–21]; these kernels, along with the local PNG contribution, are included in [Appendix D](#) for completeness. The integrated contribution to the number counts contains the integrated Sachs-Wolfe effect (ISW), Shapiro

³This is equivalent to assuming the local plane-parallel, constant redshift limit.

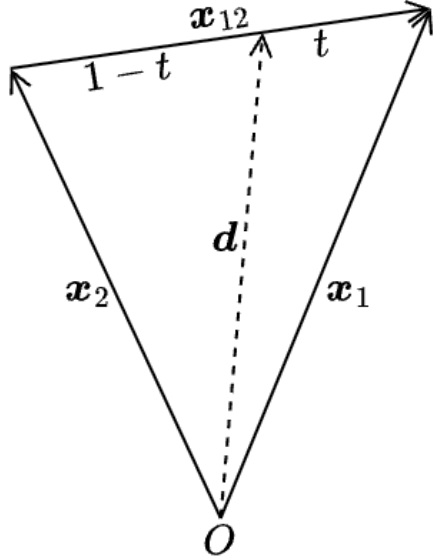


Figure 1: Geometry of the local 2-point function described by a single LOS, \mathbf{d} where t describes its choice along the vector \mathbf{x}_{12} .

time delay (TD), and lensing effects (L) instead are

$$\mathcal{K}^L(\mathbf{q}, \mathbf{x}, r) = 3 D(r) (\mathcal{Q} - 1) \Omega_m(r) \mathcal{H}^2(r) \frac{(x - r) r}{x} \left[1 - (\hat{\mathbf{q}} \cdot \hat{\mathbf{x}})^2 + 2 i \frac{(\hat{\mathbf{q}} \cdot \hat{\mathbf{x}})}{r q} \right], \quad (2.11a)$$

$$\mathcal{K}^{TD}(q, x, r) = 6 D(r) (\mathcal{Q} - 1) \frac{\Omega_m(r) \mathcal{H}^2(r)}{q^2 x}, \quad (2.11b)$$

$$\mathcal{K}^{ISW}(q, x, r) = 3 D(r) \left[b_e - 2 \mathcal{Q} + \frac{2(\mathcal{Q} - 1)}{x \mathcal{H}} - \frac{\mathcal{H}'}{\mathcal{H}^2} \right] \frac{\Omega_m(r) \mathcal{H}^3(r) (f(r) - 1)}{q^2}, \quad (2.11c)$$

where \mathcal{H} the conformal Hubble parameter, D is the linear growth function, f is the linear growth rate and $'$ refers to a derivative with respect to conformal time (\mathcal{Q} and b_e are defined below). Functions of r here are therefore evaluated along the integrand from observer to source while the other functions are evaluated at the redshift of the source, x , e.g. $\mathcal{Q} \equiv \mathcal{Q}(x)$; note that the integrand itself is pure cosmology and independent of tracer but has bias dependence only in the prefactors. The total integrated contribution to the galaxy number counts can then be written as

$$\mathcal{K}^I(\mathbf{q}, \mathbf{x}, \mathbf{r}) = \mathcal{K}^L(\mathbf{q}, \mathbf{x}, r) + \mathcal{K}^{TD}(q, x, r) + \mathcal{K}^{ISW}(q, x, r). \quad (2.11d)$$

We could also re-express these kernels in terms of scalar quantities if $\mathbf{x} \equiv \mathbf{d}$, such that these kernels can be expressed in terms of q, μ, d, r . These kernels are dependent on the luminosity function through \mathcal{Q} and b_e which are defined with respect to the luminosity cut for a flux limited survey,

$$b_e = -\frac{\partial \ln n_g}{\partial \ln(1+z)} \Big|_c, \quad \mathcal{Q} = -\frac{\partial \ln n_g}{\partial \ln L} \Big|_c, \quad (2.12)$$

where L is the luminosity, n_g is the co-moving number density and $|_c$ refers to an evaluation at the flux cut; see [32] for a more detailed overview.

Therefore, the local 2-point function, can be expressed an expansion over all contributions such that,

$$\xi_{\text{loc}}(\mathbf{x}_1, \mathbf{x}_2) \equiv \langle \Delta(\mathbf{x}_1) \Delta(\mathbf{x}_2) \rangle = \sum_{\alpha, \beta \in \{\text{S}, \text{NI}, \text{I}\}} \langle \Delta_g^\alpha(\mathbf{x}_1) \Delta_g^\beta(\mathbf{x}_2) \rangle. \quad (2.13)$$

In the next section we derive the $\text{I} \times \text{I}$ contribution, which has been previously been neglected, to the local power spectrum. A brief summary of the $\text{I} \times \text{S}$ contribution in our framework is also included in [Appendix C](#). The local relativistic, Kaiser and local PNG terms are also computed [e.g. 51, 60] with the inclusion of wide-separation (wide-angle and radial evolution) corrections.

2.2 Integrated Contributions to the Local Power Spectrum

The $\text{I} \times \text{I}$ contribution to the local 2-point correlation can be expressed as

$$\langle \Delta^{\text{I}}(\mathbf{x}_1) \Delta^{\text{I}}(\mathbf{x}_2) \rangle = \int_{\mathbf{q}} \int_0^{x_1} dr_1 \int_0^{x_2} dr_2 e^{i \mathbf{q} \cdot (\mathbf{r}_1 - \mathbf{r}_2)} \mathcal{K}^{\text{I}}(\mathbf{q}, \mathbf{x}_1, r_1) \mathcal{K}^{\text{I}}(-\mathbf{q}, \mathbf{x}_2, r_2) P(q), \quad (2.14)$$

where $P(k)$ is our linear matter power spectrum and we have a double integral from the observer to source for r_1 and r_2 .

Similar to as one would in the non-integrated case, we can then switch our coordinates using $\mathbf{r}_1 = \frac{r_1}{x_1} \mathbf{x}_1$, $\mathbf{r}_2 = \frac{r_2}{x_2} \mathbf{x}_2$ and $\mathbf{x}_1 = \mathbf{d} + t \mathbf{x}_{12}$, $\mathbf{x}_2 = \mathbf{d} - (1-t) \mathbf{x}_{12}$ to re-express the exponential in terms of r_1 , r_2 , \mathbf{d} and \mathbf{x}_{12} as

$$\begin{aligned} e^{i \mathbf{q} \cdot (\mathbf{r}_1 - \mathbf{r}_2)} &= e^{i \mathbf{q} \cdot (\frac{r_1}{x_1} \mathbf{x}_1 - \frac{r_2}{x_2} \mathbf{x}_2)} \\ &= e^{i (\frac{r_1}{x_1} - \frac{r_2}{x_2}) (\mathbf{q} \cdot \mathbf{d})} e^{i (\frac{r_1}{x_1} t + (1-t) \frac{r_2}{x_2}) (\mathbf{q} \cdot \mathbf{x}_{12})}. \end{aligned} \quad (2.15)$$

It is then convenient to introduce the new integration variables, $y_1 = r_1/x_1$ and $y_2 = r_2/x_2$, such that the local 2-point function can be written as

$$\begin{aligned} \langle \Delta^{\text{I}}(\mathbf{x}_1) \Delta^{\text{I}}(\mathbf{x}_2) \rangle &= \int_{\mathbf{q}} \int_0^1 dy_1 \int_0^1 dy_2 (x_1)(x_2) e^{i(y_1 - y_2)(\mathbf{q} \cdot \mathbf{d})} e^{i(y_2 + t(y_1 - y_2))(\mathbf{q} \cdot \mathbf{x}_{12})} \\ &\quad \times \mathcal{K}^{\text{I}}(\mathbf{q}, \mathbf{x}_1, x_1 y_1) \mathcal{K}^{\text{I}}(-\mathbf{q}, \mathbf{x}_2, x_2 y_2) P(q). \end{aligned} \quad (2.16)$$

To form the local power spectrum with a single Fourier transform over \mathbf{x}_{12} , we then perform our wide-separation series expansion in $\epsilon = x_{12}/d$ about the point \mathbf{d} , such that we can remove the \mathbf{x}_{12} dependence from the integral. Here, we just assume the zeroth order term, $\epsilon \rightarrow 0$,⁴ but we could Taylor expand up to any order and compute wide-separation corrections, using the standard framework [51, 58]. Using the definition of the local power spectrum, [Eq. \(2.8\)](#),

⁴This is equivalent to enforcing translation invariance/statistical homogeneity in the statistics of the local 2-point function or assuming the plane-parallel, constant redshift limit in the case of the local contributions but not so when we have integrated contributions due to them breaking translation invariance outside the Limber approximation.

the $I \times I$ contribution to the local power spectrum can be written as a Fourier transform of our local 2-point function

$$P_{\text{loc}}^{\text{I}\times\text{I}}(\mathbf{k}; \mathbf{d}) = \int_0^1 dy_1 \int_0^1 dy_2 \int_{\mathbf{q}} e^{i(y_1-y_2)(\mathbf{q} \cdot \mathbf{d})} \int_{\mathbf{x}_{12}} e^{-i\{\mathbf{k} - [y_2 + t(y_1-y_2)] \mathbf{q}\} \cdot \mathbf{x}_{12}} \\ \times d^2 \mathcal{K}^{\text{I}}(\mathbf{q}, \mathbf{d}, d y_1) \mathcal{K}^{\text{I}}(-\mathbf{q}, \mathbf{d}, d y_2) P(q). \quad (2.17)$$

As there is now no \mathbf{x}_{12} dependence left in the kernels, the \mathbf{x}_{12} integral therefore becomes a Dirac-delta. Then, using

$$\delta_D^3(\mathbf{k} + A\mathbf{q}) = A^{-3} \delta_D(A^{-1}\mathbf{k} + \mathbf{q}) \quad (2.18)$$

and defining the function $G(y_1, y_2) = [y_2 + t(y_1 - y_2)]$, we can then simplify such that

$$P_{\text{loc}}^{\text{I}\times\text{I}}(\mathbf{k}; \mathbf{d}) = \int_0^1 dy_1 \int_0^1 dy_2 \int_{\mathbf{q}} e^{i(y_1-y_2)(\mathbf{q} \cdot \mathbf{d})} d^2 G(y_1, y_2)^{-3} \delta_D(\mathbf{q} - G(y_1, y_2)^{-1} \mathbf{k}) \\ \times \mathcal{K}^{\text{I}}(\mathbf{q}, \mathbf{d}, d y_1) \mathcal{K}^{\text{I}}(-\mathbf{q}, \mathbf{d}, d y_2) P(q). \quad (2.19)$$

Closing the Dirac-deltas, the $I \times I$ contribution to the local power spectrum can then be expressed as a double integral,

$$P_{\text{loc}}^{\text{I}\times\text{I}}(k, \mu; d) = \int_0^1 d y_1 \int_0^1 d y_2 e^{i(y_1-y_2) k \mu d/G(y_1, y_2)} d^2 G(y_1, y_2)^{-3} \mathcal{K}^{\text{I}}(G(y_1, y_2)^{-1} k, \mu, d, y_1) \\ \times \mathcal{K}^{\text{I}}(G(y_1, y_2)^{-1} k, -\mu, d, y_2) P(G(y_1, y_2)^{-1} k), \quad (2.20)$$

where we now express the kernels in terms of scalar quantities.

The angular μ integral can then be computed analytically to get the integrated contribution to the local multipoles but the y_1, y_2 integral needs to be computed numerically, the details of which are discussed in [Appendix G](#). Note that as $G(y_1, y_2)$ has a range of $(0, 1)$ over the 2D integrand, the integral includes all k -scales above the measured k -mode. We consider the impact of non-linear modelling and k_{max} in [Section 4.1.1](#).

2.2.1 LOS Dependence of the Local Power Spectrum

The theoretical integrated contribution to the local power spectrum ([Eq. \(2.20\)](#)) is therefore dependent on the LOS choice in the local 2-point function, due to the t -dependence of the $G(y_1, y_2)$ factor. This is only removed if we consider a Limber approximation⁵ and indeed one can see only the diagonal part, where $y_1 = y_2$, of the $I \times I$ integrand (see [Fig. 16](#)) is translation invariant. For the off-diagonal parts, the integrand correlates different redshifts which breaks the $y_1 \leftrightarrow y_2$ symmetry and as such this contribution is not translation invariant and one can therefore consider this to be a wide-separation type effect (i.e. it derives from breaking local translation invariance at large separations), even though this arises even in the zeroth order term in the x_{12}/d expansion.

⁵After the μ integral the $(y_1 - y_2)$ exponential can be written as a spherical Bessel function - we could then assume the Limber approximation such that

$$j_0(k d(y_1 - y_2)/G(y_1, y_2)) \rightarrow \delta_D(k d(y_1 - y_2)/G(y_1, y_2)),$$

which we expect to be valid at small scales and large redshifts. In this flat-sky limit, we have translation invariant integrated contributions and thus no t -dependence.

The Yamamoto estimator, Eq. (2.3), measures the power spectrum averaged over the survey volume. For the monopole, $\ell = 0$, this does not assume a particular LOS, it simply averages over LOS orientation as we average over the survey volume. After integrating our theoretical local power spectrum monopole over all LOS in our survey, \mathbf{d} , this survey averaged quantity will be independent of the LOS choice we assumed in our local 2-point function, as long as x_{12}/d expansion is valid. The size of this t -dependence in the local quantities is dependent on the separation and scales that are being correlated and is present in all wide-separation type terms.

Beyond the monopole, the LOS choice also dictates the vector about which we decompose our multipoles - see discussion of LOS choice in Section 3 - which induces additional LOS dependence in the observed power spectrum multipoles and as such these survey averaged multipoles are indeed dependent on the LOS choice, unlike in the monopole. Therefore, for $\ell > 0$ the LOS choice is important and indeed, as the natural choice of LOS for the Yamamoto estimator is an endpoint LOS, it is important one calculates the corresponding endpoint LOS theory.

A major consequence of this is that the leading order integrated terms generate non-zero, imaginary, odd-parity multipoles to the auto-power spectrum for $t \neq 1/2$ ⁶. While this is a novel result, we reiterate that this signal should be considered a wide-separation type contribution - akin to the more well studied dipole from wide-separation corrections to the Kaiser contribution. The integrated contributions for the even and odd multipoles are plotted in Fig. 2 and Fig. 3 and we further discuss the nature of the LOS dependence on large scales in Appendix F.

2.3 Survey Power Spectrum Multipoles

To get the theoretical expectation of the power spectrum multipoles we measure with the estimator, we must average our local power spectrum over our survey volume. In the standard literature, we can extract the local multipoles by averaging over μ the local power spectra with the appropriate Legendre polynomial

$$P_{\ell,\text{loc}}^{ab}(k; d) = \frac{(2\ell + 1)}{2} \int_{-1}^1 d\mu P_{\text{loc}}^{ab}(k, \mu, d) \mathcal{L}_\ell(\mu), \quad (2.21)$$

and finally we can obtain the theoretical power spectrum multipole of the survey by averaging the local power spectrum multipoles over the survey volume

$$\hat{P}_\ell^{ab}(k) = \int_V \frac{d^3 \mathbf{d}}{V} P_{\ell,\text{loc}}^{ab}(k; d), \quad (2.22)$$

as in Eq. (2.7). However, to correctly do this averaging over \mathbf{d} for wide-separations we need to properly account for the LOS dependence in our 2-point function in our averaging - by pair counting over all the points we are correlating; for different LOS choices we sample over slightly different redshifts. Further consideration of this averaging is left to Appendix F.

3 Forecast Setup

Throughout this study, we assume a fiducial cosmology from the Planck results [69] and we also adopt Planck constraints as priors on our cosmological parameters. We also assume a

⁶ $t = 1/2$ preserves the $y_1 \leftrightarrow y_2$ symmetry and as such the sum off-diagonal odd multipole signal cancels.

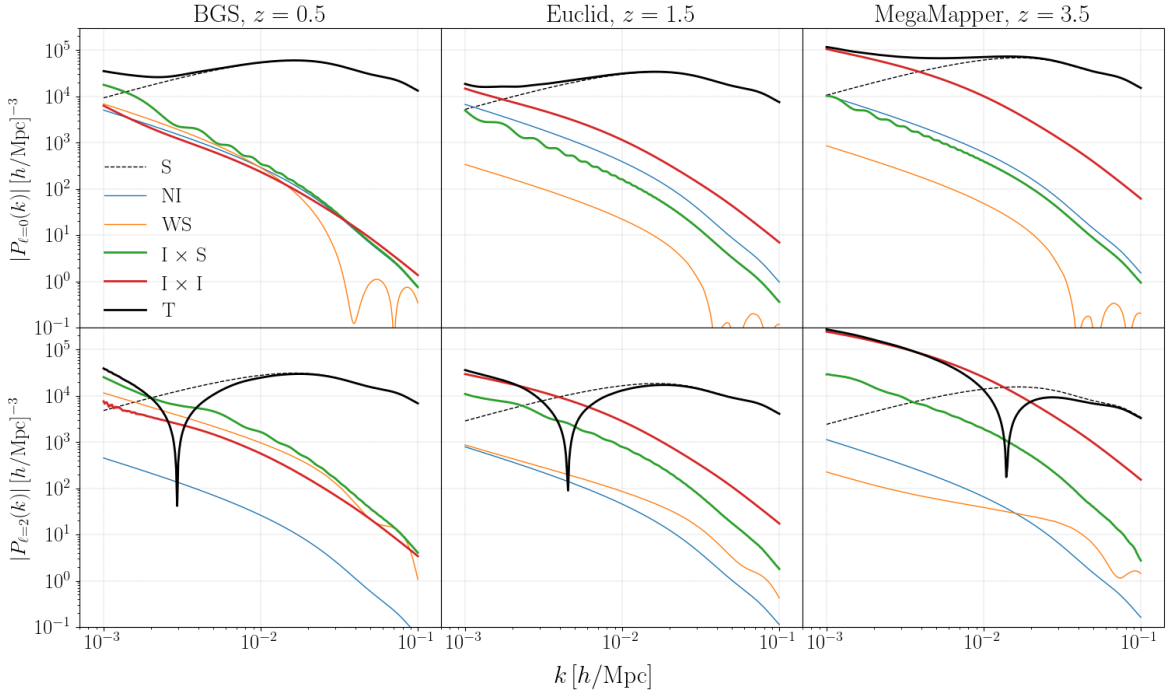


Figure 2: Monopole (top row) and the quadrupole (bottom row) of the power spectrum for each term over three different survey setups at set redshifts, with the standard Kaiser power spectrum shown in black (dashed).

fiducial value of $f_{\text{NL}} = 0$. Bias modelling for each survey is outlined in Section A. To include the uncertainty on our bias parameters (b_1 , \mathcal{Q} , b_e) we introduce and marginalize over bias amplitude parameters, α_{b_x} , such that $b_1 \rightarrow \alpha_{b_1} b_1$, $\mathcal{Q} \rightarrow \alpha_{\mathcal{Q}} \mathcal{Q}$, $b_e \rightarrow \alpha_{b_e} b_e$. Therefore, we assume we know the redshift evolution of each bias parameter but not its overall amplitude.

In the multi-tracer case (see Section A.1 for details) we now marginalise over double the number of nuisance parameters – as we model both the bright and faint samples, e.g., $b_1^B \rightarrow \alpha_{b_1}^B b_1^B$, $b_1^F \rightarrow \alpha_{b_1}^F b_1^F$. The bright and faint biases are correlated and indeed we could also include the additional information from the total sample in our analysis [e.g. 70] (so have three auto-correlations and three cross-correlations for each multipole) without adding any extra free parameters, as the biases of the total sample are fully constrained from the bright and faint values - see Equations (A.5), but we leave this extension to future work.

To model the scale-dependent bias induced by local type PNG, see Appendix D, we make the standard assumption of universality of the mass function, [10], such that b_ϕ can be linearly related to the linear bias, b_1 ⁷. We do not account for any uncertainty or try to constrain b_ϕ ; therefore, we are actually constraining $b_\phi f_{\text{NL}}$ not f_{NL} . This is a non-trivial degeneracy to break without strict theoretical priors on b_ϕ [75] however it motivates using different approaches, such as higher order statistics like the bispectrum [e.g. 76] or multi-tracer techniques [e.g. 45, 46] to help break this degeneracy.

The LOS choice in our theory is informed by two things [for a more detailed overview see

⁷While this is a simplistic assumption and is not expected to hold for real-life galaxies in most scenarios [71–74], our main focus here is modelling light-cone effects and as such we leave more detailed analysis of PNG to future work.

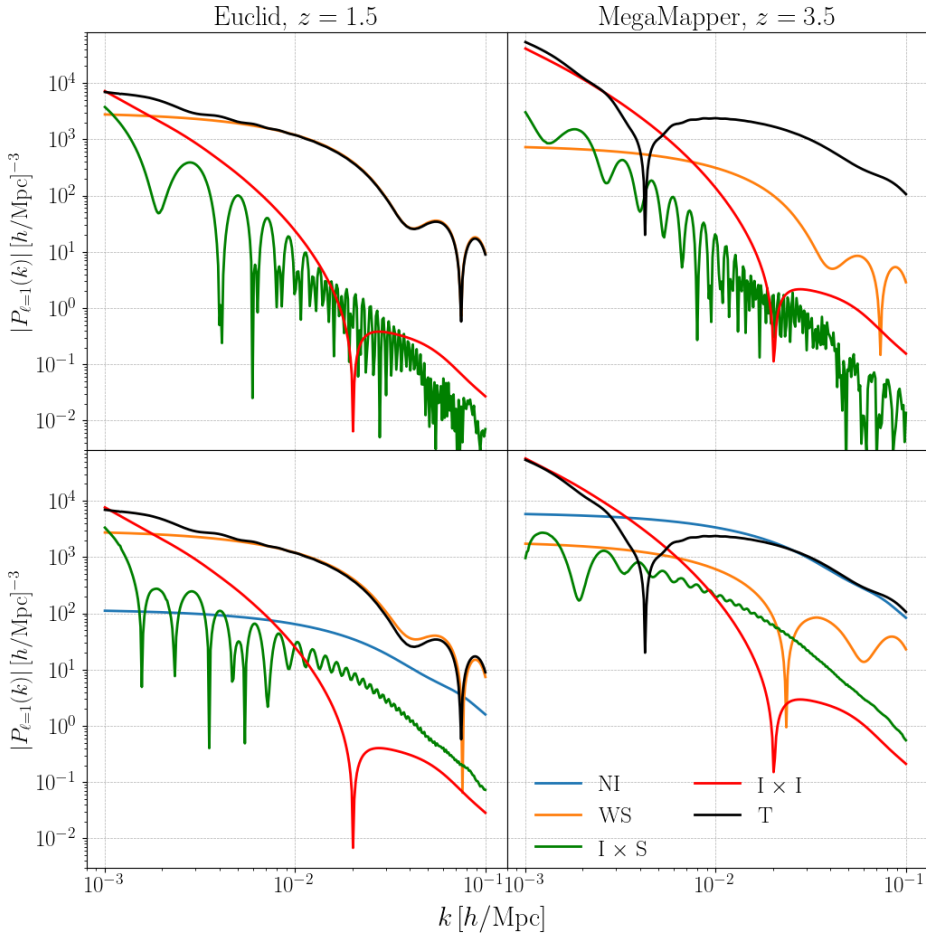


Figure 3: Imaginary dipole contribution for the bright-faint split cross-power spectrum of *Euclid* (left) ($F_c = 2 \times 10^{-16}$ [erg cm $^{-2}$ s $^{-1}$]) and MegaMapper-like ($m_c = 24$) (right) surveys. The single tracer contribution to the dipole for the integrated contributions is also shown for the same flux/magnitude cuts in the bottom two graphs.

[58]. First, it defines the point about which we perform our wide-separation expansion (this is relevant for the integrated contributions - see Section 2.2.1) to approximate the full local 2-point function, and second, it sets the vector about which we decompose our multipoles. When we measure our power spectrum over one survey, we naturally include the full LOS information of each point (we only do a perturbative expansion in our theory to approximate this) and therefore the choice of LOS in our estimator only affects our multipole decomposition. As the Yamamoto estimator is computable with separable FFTs only in the case of an endpoint LOS ($t = 0$ or $t = 1$), we use $t = 0$ as our LOS for the $\ell > 0$ multipoles. However, the monopole is not decomposed with respect to a LOS (there is no LOS dependence in the monopole estimator); it is simply the average over all LOS orientation angles, μ . Therefore, we choose the midpoint LOS $t = 1/2$ for the monopole in our analysis as it is a natural choice of LOS about which to Taylor expand our theory.

Our full data vector, D , is a sum over redshift bins (which we assume are independent), where for each redshift bin we have a data vector, D_z , containing the power spectrum

multipoles $\{\ell_i, \dots, \ell_n\}$:

$$D_z = \{P_{\ell_i}, \dots, P_{\ell_n}\}. \quad (3.1)$$

For each multipole, in k -space, we impose bin widths of $\Delta k = k_f$ with a maximum scale of k_f , where k_f is the fundamental frequency of the survey ($k_f = (2\pi)/V^{1/3}$) and, for simplicity, a cut-off scale at $k_{\max} = 0.15 [h/\text{Mpc}]$, unless stated otherwise. We also impose an additional effective k_{\min} by excluding Fourier modes where $k < 2\pi/x(z_{\min})$ for the minimum redshift included in the bin, as above these scales we expect the perturbative wide-separation expansion to have broken down.

In our single tracer analysis our usual data vector for each bin is $\ell = 0, 2, 4$ and in the full multi-tracer analysis, the data vector for each multipole is larger, $P_{\ell_i=\text{even}} = \{P_{\ell_i}^{BB}, P_{\ell_i}^{BF}, P_{\ell_i}^{FF}\}$ as we have both our bright, B and faint, F , samples. In addition, in the multi-tracer case one can now also consider the odd multipoles ($\ell = 1, 3$) as well, however the auto-correlations are still zero and therefore we only include the cross-correlations for the odd multipoles, $P_{\ell_i=\text{odd}} = P_{\ell_i}^{BF}$.

To quantify both the constraints on a particular parameter, in this case f_{NL} , and the bias on the maximum likelihood value if we ignore particular effects, we can either adopt a Fisher matrix formalism, [e.g. see 77], or we can sample the full likelihood function directly with a full Markov chain Monte Carlo (MCMC) pipeline. Fisher matrices are fast and easily reproducible but they only compute the likelihood at the fiducial point in parameter space and they assume Gaussianity in the parameter covariance. Therefore, for large parameter biases and non-Gaussian, degenerate posteriors we would expect Fisher matrices to not fully describe the true nature of the parameter space. Therefore, we initially adopt an MCMC formalism but when we include integrated effects in our modelling then this becomes significantly more computationally expensive and so we revert to Fisher forecasts, though we note that the MCMC posteriors appear largely Gaussian. A brief summary of both methods is provided below.

MCMCs Our likelihood function is given by

$$\log(\mathcal{L}) \propto (D^{\text{True}}(\theta_0) - D(\theta))^{\dagger} C^{-1} (D^{\text{True}}(\theta_0) - D(\theta)), \quad (3.2)$$

where $D^{\text{True}}(\theta_0)$ is the full ‘True’ theory evaluated at the fiducial parameter, θ_0 and $D(\theta)$ is our incomplete theory where we have neglected some contributions. Therefore, we evaluate $D(\theta_i)$ for each sample in parameter space, θ_i .

We use the MCMC sampler implemented in the public code COBAYA [78–80]. To efficiently sample over the cosmological parameter space, we use the power spectrum emulators from COSMOPOWER [81], which in the case of the non-linear power spectrum is emulated from results of HMCODE [82]. For all chains the tolerance for convergence is set by the Gelman-Rubin parameter $R - 1 = 0.001$.

Fisher Matrices The Fisher information matrix is defined as

$$F_{ij} = \left(\frac{\partial D}{\partial \theta_i} \right)^{\dagger} (C^{-1})_{ij} \frac{\partial D}{\partial \theta_j}, \quad (3.3)$$

where we have partial derivatives of the data vector with respect to each parameter.

If we use an incomplete model, $D(\theta)$, in our analysis where we have neglected some correction to our observable then our parameter inference will be biased from ‘True’ value, or in this case fiducial value, θ_0 . Here our data vector, D , is evaluated solely at the fiducial

values in parameter space, θ_0 . With the assumption of a Gaussian likelihood, the predicted bias in the maximum likelihood value, with respect to the true value of a given parameter θ_i , is given by [83–85]

$$\Delta\theta_i = (F_{ij})^{-1}B_j \quad (3.4)$$

where

$$B_j = \left(\frac{\partial D}{\partial \theta_j} \right)^\dagger (C^{-1})(D^{\text{True}}(\theta_0) - D), \quad (3.5)$$

and $D^{\text{True}}(\theta_0)$ is our complete theory model. Note that we use the conditional errors, not marginalised errors, to compute the bias.

4 Results and Discussion

This section is structured as follows: first we discuss the nature of the integrated contribution to the power spectrum, secondly we explore bias in the determination of f_{NL} if one neglects different corrections in their analysis, [Section 4.2](#), and lastly we discuss the forecasted constraints on f_{NL} when we need to account for uncertainty in our luminosity function, [Section 4.3](#), and how this situation improves if we consider a multi-tracer approach, [Section 4.3.1](#).

4.1 Integrated Contributions to the Power Spectrum

Here we briefly discuss the nature of the different light-cone corrections to the power spectrum multipoles; though we stress these results are not only scale-, tracer- and redshift-dependent but also on the specific bias modelling adopted.

Even Multipoles The absolute values of the integrated contributions to the even multipoles are plotted alongside the other terms in [Fig. 2](#). For the lower redshift DESI-like BGS sample one can observe that the integrated light-cone contributions ($I \times I$ and $I \times S$) are comparable to the local, local relativistic (NI) and wide-separation (WS) corrections (note this is dominated by the wide-angle part for low redshifts), with the same $\approx 1/k^2$ dependence. For the higher redshift *Euclid*-like H α and MegaMapper-like LBG samples, the $I \times I$ is the leading light-cone correction and indeed, it is even larger, particularly in the MegaMapper case, than the Kaiser contribution for ultra-large, post-equality, scales. The $I \times S$ contribution is a similar order of magnitude to the local relativistic contribution in the monopole but is roughly an order of magnitude larger in the quadrupole. Most of the contributions are positive, except for the local relativistic term and the wide-angle corrections to the Kaiser terms.

Wide-separation corrections (WS) here are generally subdominant to the other light-cone corrections beyond $z = 1$; the wide-angle correction to the Kaiser terms have a $1/(kd)^2$ dependence so at higher redshifts the wide-separation contribution is predominantly caused by radial evolution corrections, however this remains subdominant to the other light-cone effects. Generally, the most important wide-separation contribution here is the first order correction to the (\mathcal{H}/k) odd parity local relativistic term.

Odd Multipoles In the single tracer case, the odd multipoles are purely generated by the contributions to the local power spectrum which break translation invariance, see top panel of [Fig. 3](#) - this includes the off-diagonal parts of the integrated contributions. These contributions, as expected peak on large scales, and while the wide-separations corrections

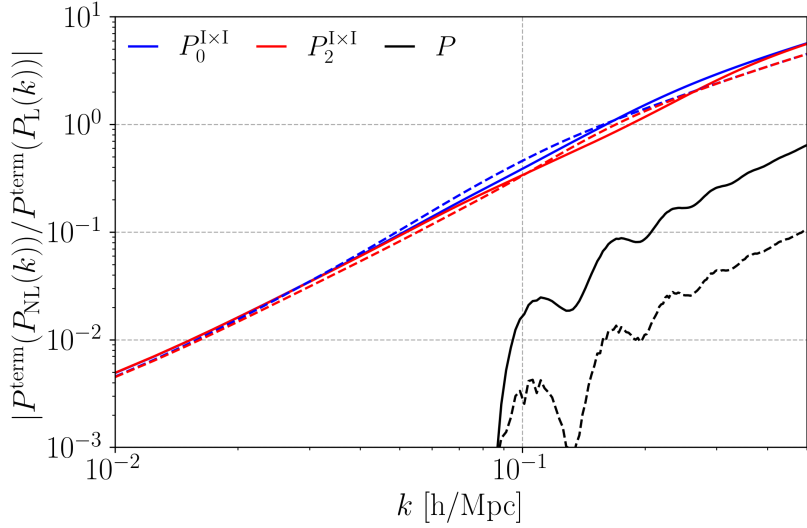


Figure 4: Ratio of power spectrum contributions when using a non-linear $P(k)$ (HMcode) modelling compared to using linear $P(k)$. The solid lines represent a $z = 1$ *Euclid*-like survey while the dashed lines represent a MegaMapper-like LBG survey at $z = 3$. Other than the $I \times I$ term, all contributions are simply proportional to the ratio of the non-linear to the linear power spectra which is represented in black.

to Kaiser terms are more dominant for *Euclid*, the integrated contributions become more relevant at higher redshifts.

However, when we cross-correlate two samples with different biases, this break in symmetry generates a non-zero imaginary contribution to the odd multipoles even in both the plane-parallel constant rredshift and Limber approximations. Fig. 3 shows the dipole ($\ell = 1$) for bright-faint splits for *Euclid* and MegaMapper-like surveys. For the local terms, the wide-separation contributions, are dominated by the first order (x_{12}/d) corrections to the Kaiser term. These are of the same order of magnitude as the leading order (\mathcal{H}/k) local relativistic effects, wide-separation tends to be larger for *Euclid* but smaller for MegaMapper, and they also have the same general $1/k$ dependence. The integrated contributions have a steeper k dependence and so are particularly relevant on ultra-large scales as well as at higher redshifts. The $I \times I$ term in particular, is suppressed and has a negligible impact to the odd multipoles above $k \approx 0.01 h/\text{Mpc}$ but theoretically would be leading contribution to the dipole at $k = 0.001 h/\text{Mpc}$.

4.1.1 Non-linear Contributions to the Integrated Effects

As the integrand in Eq. (2.20), is a function of $k/G(y_1, y_2)$ - rather than just k - where $G(r_1, r_2, d)$ has a range of $(0, 1)$, the integrand is dependent on all k -modes where $k' < k$. The $I \times I$ contribution is therefore sensitive to non-linear effects even when considering large linear scales. To explore the nature of this non-linear dependence, we consider a simple model of including non-linear effects where we replace the linear matter power spectrum with the non-linear one, $D(x_1)D(x_2)P(k) \rightarrow P_{NL}(k, x_1, x_2)$, where x_1, x_2 could be d , or r_1, r_2 if we are considering an integrated term (to quantify the non-linear power spectrum from two unequal redshifts of the density field, as in the integrated case, we use the mean redshift). Although this is a simplified treatment of including non-linear effects, it illustrates their impact on the

integrated contributions at even very mildly non-linear scales. When considering the ratio of each contribution using a non-linear, $P_{NL}(k)$ compared to using the linear, $P(k)$, (Fig. 4) we can see that for nearly all terms, including the I×S contribution as this is dominated by the part of the integrand at the source (see discussion in Appendix G), are simply the ratio of the two power spectra but for the I×I contribution there is a significant increase in the signal even at low k - we find about a 10% boost in the signal from the non-linear power spectrum at $k = 0.05 h/\text{Mpc}$, for both MegaMapper and *Euclid*. This non-linear boost is of the order of 100% at $k = 0.15$ and also appears somewhat independent of redshift (as *Euclid* and MegaMapper receive similar boosts) compared to power spectrum itself which becomes more linear at higher redshifts; this behaviour for the I×I can be understood as the integrand is sensitive to smaller scales as it samples the lower redshift power spectrum closer to observer. We consider the potential bias from the non-linear boost to the I×I term in Appendix E.

4.2 Bias on Inference of PNG

We now quantify the bias (shift) in the inferred value of the local type f_{NL} that arises when specific light-cone systematics are neglected in the analysis. The forecast setup and the details of the computation of the bias on the best fit value is described in Section 3. When forecasting the bias in this section we do so to mimic a naive analysis that completely neglects these corrections and so therefore, we also do not include the effect of these correction on the covariance; the covariance is simply the Kaiser sample variance plus shot-noise. Therefore the error on f_{NL} only changes when we investigate the bias from neglecting different effects as we are sampling different areas of parameter space and the slight variation in convergence of chains.

Fig. 5 shows the bias induced by local relativistic and wide-separation terms is of $\Delta f_{NL} \sim \mathcal{O}(1) \sigma$ for *Euclid*, SKA and MegaMapper-like surveys after marginalising over α_{b_1} (values are printed in Table 1). For the BGS and Roman-like surveys, this bias is within the survey error bars; constraints on f_{NL} are quite closely linked to the observed volume, as larger volumes not only allows for a greater number of k -modes (bin width is set by k_f and therefore the volume) but also because the f_{NL} signal is greater on large scales. The constraints for BGS and Roman are therefore weakened by their small redshift range and observed sky fraction, respectively. While this bias is dominated by the pure local relativistic contribution, the most important wide-separation term is the 1st order wide-separation corrections to the \mathcal{H}/k odd local relativistic contribution which then enters the even multipoles. Wide-angle effects are more relevant at low redshift with a bias of $\Delta f_{NL} \approx \mathcal{O}(1)$ for the DESI-like BGS survey from neglecting wide-separation effects despite different contributions of the wide-separation term shifting f_{NL} in opposing directions.

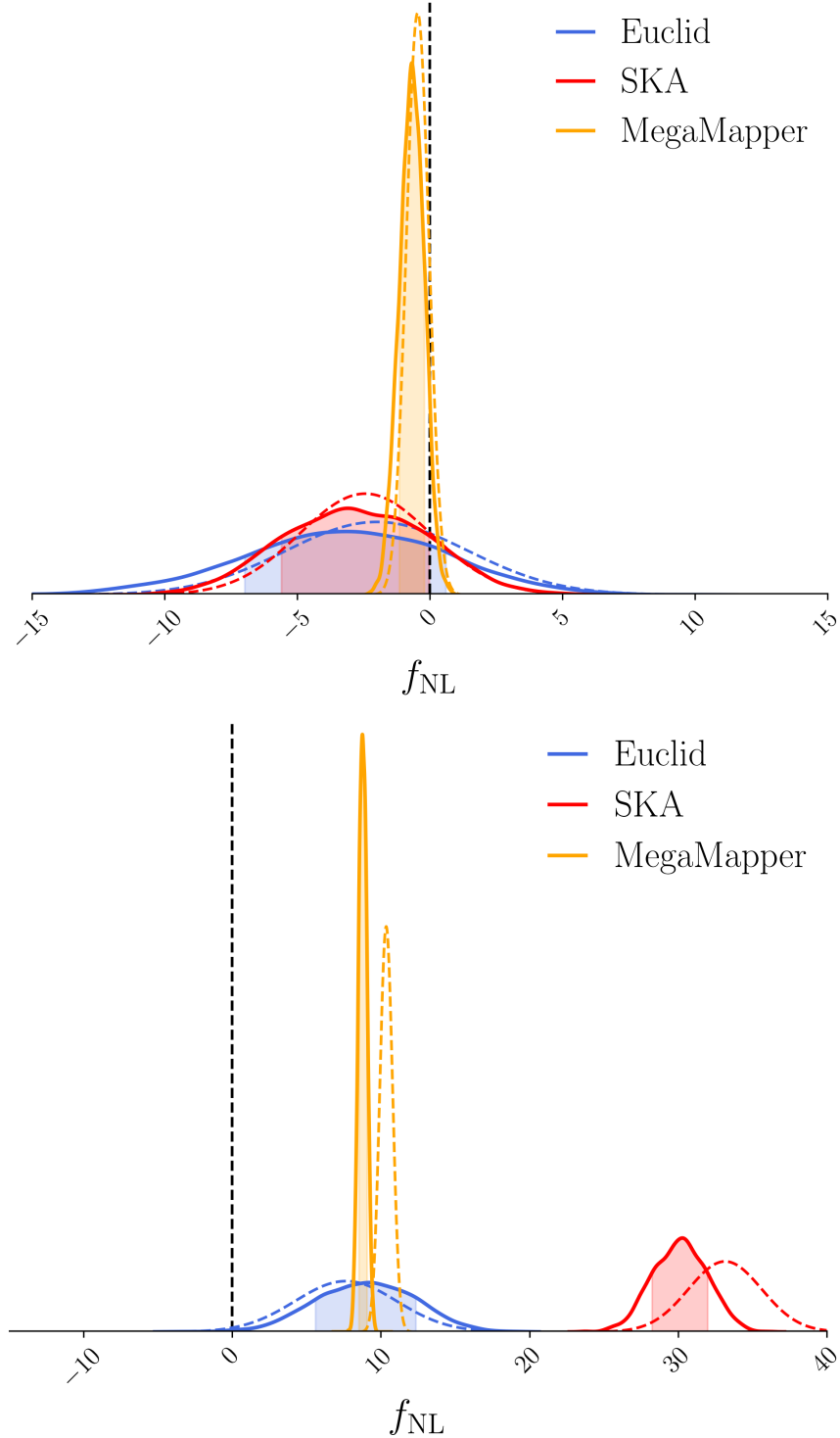


Figure 5: PDF of the forecasted constraints on local f_{NL} for a fiducial value of $f_{\text{NL}} = 0$, after marginalising over α_{b_1} , using a MCMC analysis (solid lines) and a Fisher analysis (dashed lines). Top panel considers the case where local relativistic effects and wide-separation corrections are ignored while the bottom panel considers the case where local relativistic, wide-separation and the integrated contributions are all neglected.

Table 1: Constraints on local type f_{NL} , for a fiducial $f_{\text{NL}} = 0$ if we neglect selected theoretical systematics in our MCMC forecast, after marginalising over α_{b_1} .

	DESI BGS	Roman	<i>Euclid</i> H α	MegaMapper	SKAO2
NI	$-3.5^{+20.8}_{-21.7}$	$-2.2^{+8.5}_{-8.4}$	$-3.2^{+4.0}_{-4.0}$	$-0.64^{+0.49}_{-0.49}$	$-3.0^{+2.8}_{-2.9}$
NI+WS	$-1.8^{+20.6}_{-20.5}$	$-1.6^{+8.5}_{-9.0}$	$-3.2^{+3.8}_{-3.8}$	$-0.68^{+0.47}_{-0.48}$	$-2.8^{+2.8}_{-2.8}$
NI+WS+I	$4.9^{+20.3}_{-21.4}$	$3.3^{+8.4}_{-8.9}$	$9.0^{+3.3}_{-3.4}$	$8.8^{+0.28}_{-0.27}$	$30.2^{+1.8}_{-1.9}$

The constraints on f_{NL} are tighter for SKAO2 and MegaMapper than they are for *Euclid*, and this can largely be attributed to the higher redshift ranges and sky fractions observed by these surveys such that they contain a higher number of modes. We can also see that for these relatively small deviations from the fiducial values the Fisher matrix approach provides a fair description of the true posterior as it generally agrees with the MCMC samples.

However, when we also consider the impact of neglecting integrated contributions, I \times I and I \times S, the bias goes from small negative values of f_{NL} to large positive values. We can understand this behaviour if we consider each contribution to the even multipoles of the power spectrum (Fig. 2), the local relativistic (and wide-angle) contributions are generally negative, suppressing power at large scales while the integrated contribution is positive, boosting power on large scales. The bias is then predominantly caused by the large I \times I contribution, and indeed if one considers the bias in each individual redshift bin, one can see a general increase with redshift as the integrated contributions are comparatively larger. The particularly large bias in the SKAO2 case can be attributed to the ratio of \mathcal{Q} and b_1 . The f_{NL} signal is proportional to b_1 but as the lensing term is proportional to \mathcal{Q} , we can see the bias is related to the ratio \mathcal{Q}/b_1 , which is larger for SKAO2 than the equivalent redshift *Euclid*-like survey, as the SKAO2 H α galaxy catalogue is a less biased sample of the underlying dark matter distribution (it has lower values of b_1).

The shift on the bias is summative for each contribution in the case of the Fisher analysis, but this is no longer true when using an MCMC analysis. Also, as the posterior is several σ away from the fiducial values, we can see the linear Fisher approximation breaks down and does not properly represent the true posterior.

We can also consider the impact of neglecting light-cone effects when we sample over cosmological parameter space. Fig. 6 shows the full MCMC chains where we do not assume a fixed cosmology, for *Euclid* (blue) and MegaMapper-like (green) surveys. The cosmological parameters (Ω_b , Ω_{cdm} , A_s , n_s) have priors drawn from the *Planck* 2018 constraints, [69] and therefore both *Euclid* and MegaMapper have smaller difference in cosmological parameter constraints, as these are bounded by tight *Planck* priors. However, A_s , even with *Planck* priors, is biased from the fiducial value in the MegaMapper case. The f_{NL} constraints, $f_{\text{NL}} = 9.39^{+3.37}_{-3.49}$ for the *Euclid*-like sample and $f_{\text{NL}} = 9.15^{+0.29}_{-0.29}$ for the MegaMapper-like sample, are largely consistent to the case where we assume a fixed cosmology. If we forgo priors on cosmology (Fig. 22), then our constraining power on f_{NL} weakens slightly for the *Euclid*-like (MegaMapper-like) sample, $f_{\text{NL}} = 10.01^{+3.53}_{-3.76}$ ($f_{\text{NL}} = 9.42^{+0.31}_{-0.33}$), due to the broader constraints on cosmological parameters. In addition, for the MegaMapper-like sample the cosmological parameter is also biased for both $\Delta(A_s) = 9.3\sigma$ and $\Delta(n_s) = 1.4\sigma$. Therefore, the biases and errors on our determination of f_{NL} appear robust to our choice of free

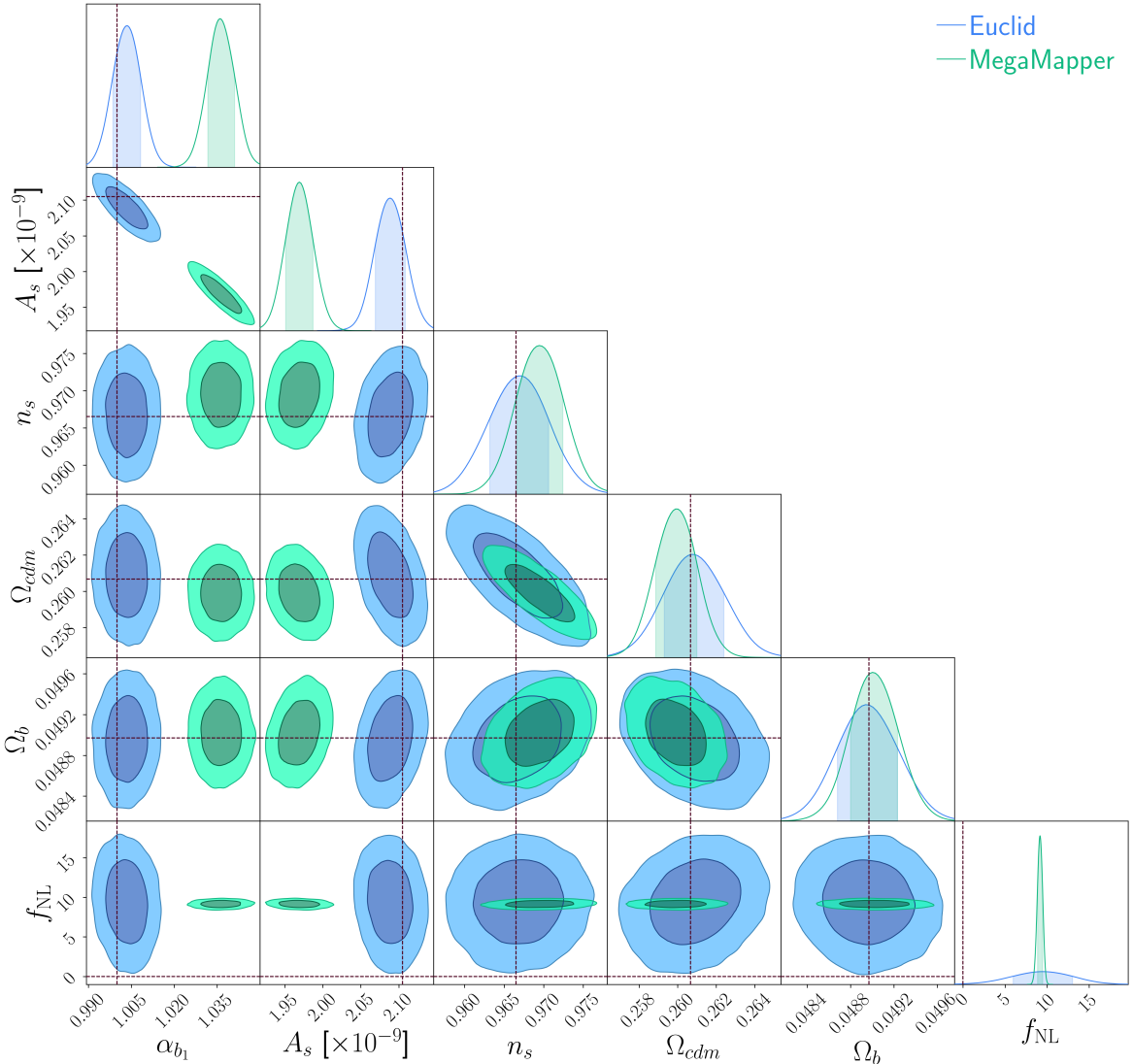


Figure 6: Forecasted marginalised and joint parameter constraints for a *Euclid*-like H α survey (blue) and a MegaMapper-like LBG survey (green), if we neglect integrated, local relativistic and wide-separation effects in our analysis. We assume Planck priors on cosmological parameters and solid colour representing the 1σ constraints and the lighter region denoting the 2σ constraints.

parameters.

4.3 Constraints on Local PNG

The constraints on f_{NL} in the previous section are comparable with previous analyses [e.g. 12, 13] which have largely ignored the impact of light-cone systematics. However, as we have shown that neglecting these effects leads to a sizeable bias in our inference of f_{NL} and other cosmological parameters, we need to include these systematics in our analysis. This impacts our constraints on f_{NL} as the relativistic terms are dependent on the survey luminosity function through the evolution and magnification bias; therefore uncertainty in our luminosity

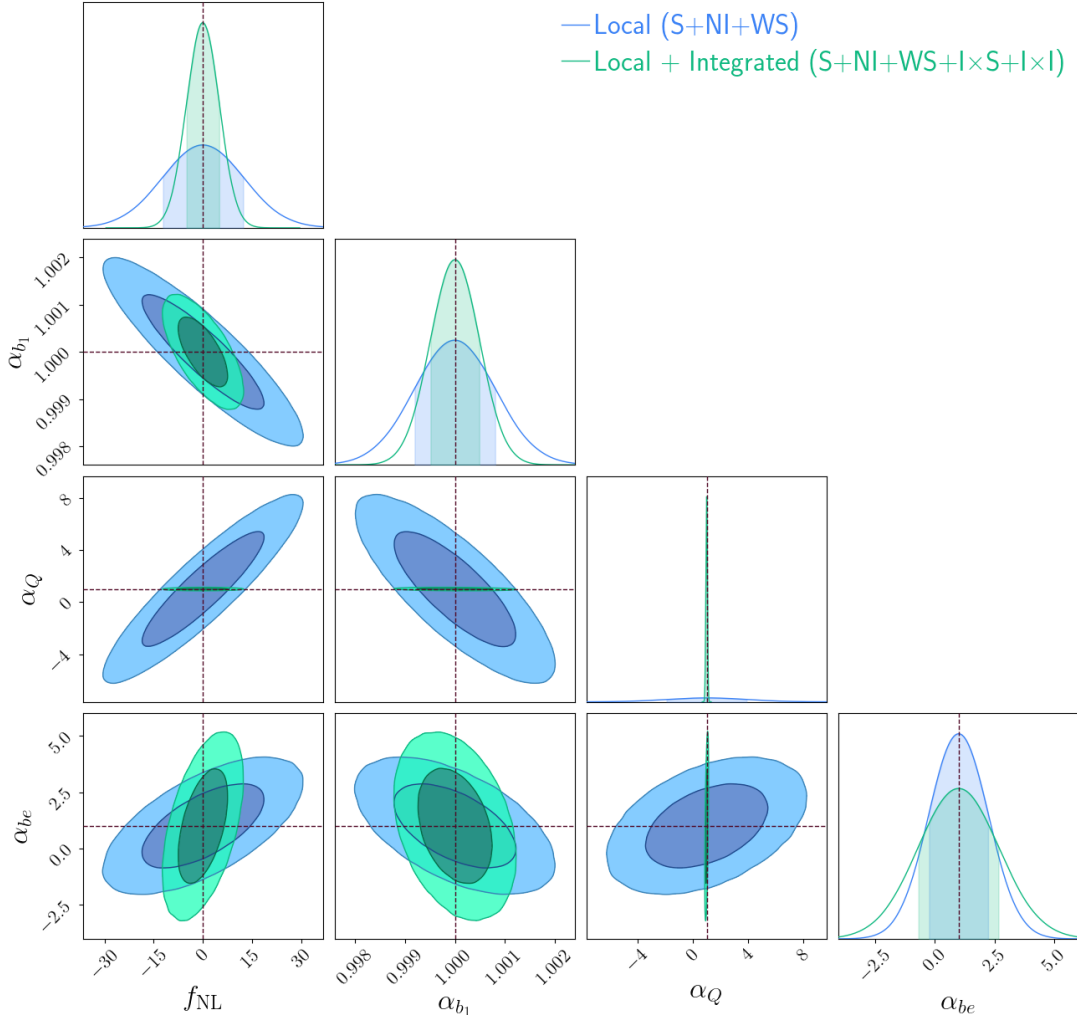


Figure 7: Fisher forecasted marginalised and joint constraints on local type f_{NL} and bias amplitude parameters for a *Euclid*-like H α survey. Ellipses are green where we only include local corrections (S+NI+WS) and blue where we also include integrated contributions (S+NI+WS+I×S+I×I).

function leads to uncertainty in our determination of f_{NL} . We account for this uncertainty by marginalising over the amplitude of the bias parameters, α_Q, α_{be} . We do not include any prior constraints on α_Q and α_{be} .

In addition, these light-cone effects also contribute to the sample variance (see Appendix B) and here the integrated contributions are relevant on larger scales and higher redshifts. This extra positive contribution therefore leads to a reduction in SNR for local type f_{NL} . In these forecasts, we include the same terms in the covariance as we do in the signal.

Table 2: Marginalised constraints on f_{NL} for a full relativistic analysis - including the uncertainty in our luminosity function.

	DESI BGS	Roman	<i>Euclid</i> H α	MegaMapper	SKAO2
$\sigma(f_{\text{NL}})$	24.3	10.1	4.6	0.49	2.9

Previous studies, such as [28, 31], have considered the impact of the uncertainty in the luminosity function on the constraints of f_{NL} , however these have not included the impact of integrated corrections. In that scenario, both \mathcal{Q} and b_e are poorly constrained by the power spectrum and therefore there is a large increase in the uncertainty on f_{NL} . However, with the additional inclusion of integrated effects, the large lensing contribution yields far tighter constraints on \mathcal{Q} and thus tighter constraints on f_{NL} than in the local effects only case. This is demonstrated for a *Euclid*-like survey in Fig. 7, with only local corrections, $\sigma(f_{\text{NL}}) = 12.0$, in blue and when including integrated effects, $\sigma(f_{\text{NL}}) = 4.5$, in green.

In order, to understand the impact of additional contributions to the covariance and the added nuisance parameters $\alpha_{\mathcal{Q}}, \alpha_{b_e}$, we can forecast the uncertainty on f_{NL} with and without the additional corrections to the covariance. However, we find that the additional corrections to the covariance has a minimal impact on the constraints on f_{NL} despite it leading to noticeably worse constraints on other bias parameters, notably $\alpha_{\mathcal{Q}}$, compared to the Newtonian covariance case. Marginalised constraints on f_{NL} for a full relativistic analysis are shown in Table 2.

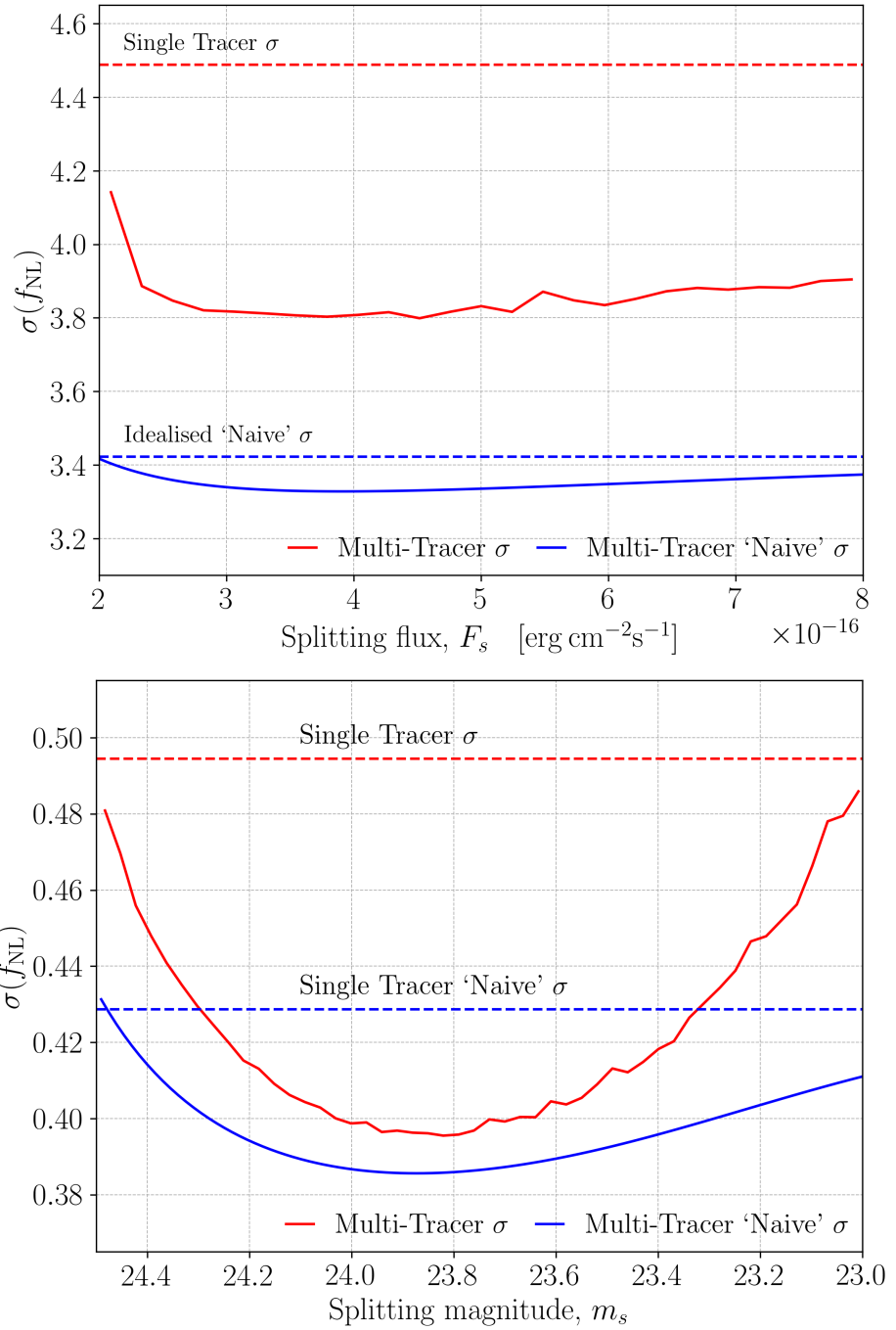


Figure 8: Fisher forecasted errors on local f_{NL} for multi-tracer (solid lines) and single tracer (dashed) analyses. The ‘naive’ analysis where one ignores light-cone corrections, including in the covariance, is shown in blue and the case where we include these corrections and the additional nuisance parameters is shown in red. Top panel is for a bright-faint split of a *Euclid*-like H α survey plotted as a function of the flux split, F_s and the bottom panel is for a MegaMapper-like LBG survey plotted as a function of apparent magnitude split, m_s .

4.3.1 Multi-Tracer Analysis

As our constraints on f_{NL} are now dependent on how well we know both \mathcal{Q} and b_e , constraints on f_{NL} will improve if we have more information about the survey luminosity function. This motivates the consideration of a multi-tracer analysis, for which there are non-cancelling odd multipoles, which are sourced, in part, by the leading order \mathcal{H}/k local relativistic corrections and further the $I \times S$ contribution is also non-negligible here - for example see Fig. 3. Therefore, the signal in the odd multipoles while not containing a local f_{NL} signal, can help break the degeneracy between \mathcal{Q} and b_e , and f_{NL} ; improved constraints on b_e is the main gain here as \mathcal{Q} is already well constrained by the large $I \times I$ contribution, for example see Fig. 7. In addition, the use of highly biased tracers can enhance the f_{NL} though the b_ϕ dependence [45–47]. We do however have more free parameters as we have to model biases for both the bright and faint populations. Details of the multi-tracer analysis are outlined in Sections 3 and A.1.

Fig. 8 shows a comparison of the forecasted constraints of f_{NL} for a few different scenarios: first, for the idealised ‘naive’ case (blue) where \mathcal{Q} and b_e are fixed and there are no relativistic or wide-separations corrections to the covariance; therefore this is what one would forecast if they ignored light-cone effects. Secondly, for the single tracer case where we account for uncertainty in \mathcal{Q} and b_e and include all the effects discussed in this work both in the signal and covariance, for $\ell = 0, 2, 4$ and lastly for the multi-tracer case where we now include not only odd multipoles ($\ell = 1, 3$) but also bright-bright, bright-faint and faint-faint auto- and cross-correlations, plotted over splitting flux/magnitude.

We can see that, adopting a bright-faint split approach, when we are modelling for light-cone effects, tightens constraints on local type f_{NL} by approximately 15 – 20% for both *Euclid* and MegaMapper-like surveys, for a sensible flux/magnitude cut, despite the fact we are marginalising over double the number of nuisance parameters. Therefore, this approach mitigates some of the uncertainty induced from parametrising the luminosity function to model relativistic effects, and indeed, for the MegaMapper-like survey the constraints are tighter than in the naive case, where we completely neglect relativistic corrections, for a sensible choice of the magnitude split. In part, the better constraints using the bright-faint split approach with MegaMapper can be explained by the fact that at high redshifts we are using highly biased tracers, which can amplify the f_{NL} signal.

5 Summary and Conclusions

The multipoles of the 3D power spectrum remains a popular basis for LSS analysis for several reasons; they are theoretically straightforward, preserve the full 3D information of the field and have an efficient estimator. However, its modelling on large scales does present a few challenges. A couple of which have been the focus on in this work; firstly, until recently integrated effects were challenging to include directly in the 3D power spectrum framework, secondly, the inclusion of wide-separation corrections which arise as we correlate objects on our past light-cone.

We therefore present a framework in which to include integrated effects—lensing, ISW and time delay—and in particular the $I \times I$ term, in the multipoles of the 3D Fourier power spectrum. This contribution requires the computation of numerical integrals from observer to source and is dominated by the lensing contribution for all but the smallest redshifts, and indeed at large redshifts and ultra-large scales (so for largest k -bins for MegaMapper) it can be the dominant contribution to the even multipoles of the power spectrum. We forecast that the lensing contribution should be detectable for *Euclid*, MegaMapper and SKAO2-like surveys,

however the ISW and time delays are unlikely to be detectable in the multipoles of the Fourier power spectrum. We have also shown that, for upcoming spectroscopic galaxy surveys, such as *Euclid* and MegaMapper, that by neglecting these terms our best fit determination of local type f_{NL} will be biased, by roughly 3σ and 20σ , respectively, from the true values and therefore these effects have to be included in an analysis. This result, while novel in the 3D power spectrum, also may be considered to be expected considering how lensing contributes to the angular power spectrum.

Therefore one has to include integrated relativistic effects, along with the local effects, in their modelling in order to perform an unbiased analysis of f_{NL} . However, to do this one needs to account for the uncertainty in the survey luminosity function through the evolution and magnification biases. To illustrate this, we again focus on a local f_{NL} analysis, in which the uncertainty in our bias functions leads to greater uncertainty ($\approx 30\%$ for a *Euclid*-like H α survey and $\approx 20\%$ for a MegaMapper-like LBG survey) in the determination of f_{NL} . Multi-tracer approaches, like a bright-faint split where we split our observed galaxy sample based on observed luminosity, can help improve constraints here. First, by increasing the relative local PNG signal by using highly biased tracers, and secondly, by giving us better constraints on the uncertainty in our luminosity function - particularly from the odd multipoles.

To enable these forecasts, we present a novel calculation of the full multipole multi-tracer covariance, including relativistic corrections, [Appendix B](#). We have for the first time, computed wide-separation corrections to the covariance which, while generally subdominant for the even multipole covariance, can be relevant on large scales for the odd-parity multipoles. Note that this is the wide-separation correction to the covariance not just the inclusion of the corrections from the power spectrum into the sample variance. This therefore involves computing wide-separation corrections to a 4-point function. We also have included integrated effects in the covariance and due to them breaking translation invariance we need to define within with respect to the LOS of our full 4-point function ([Appendix B.2](#)). Here, like in the signal, the integrated contribution becomes important on large scales and at higher redshifts. In the cross-power spectrum, odd multipoles, however, are sourced by odd imaginary contributions to the power spectrum, as well as shot noise.

In this work, we have omitted the effect of the convolution with the survey window function, which will have a significant impact the large scales considered here. The window convolution will both dampen the power on large scales as well as mix up the multipole decomposition, such that the even contribution will enter the odd multipoles, including in the covariance. The implementation and study of this needs to be considered in future work. We also have only considered linear perturbation theory and, while most of our forecasts are dominated by large scale effects, the inclusion of non-linear corrections, particularly for the I \times I term which integrates over all k -modes above the measured k (see [Section 4.1.1](#)), will be relevant in a realistic analysis. Additionally, all of our results are heavily dependent on the modelling assumptions we use for each survey, and in particular the choice of luminosity function.

Our results are implemented in the publicly available *Python* package CosmoWAP , including all of forecasts. A short tutorial notebook reproducing selected results is also provided. We plan to extend the formalism laid out here to include the shear-shear power spectrum and to higher-order statistics, such as the bispectrum.

Acknowledgments

CA and JH are supported by studentships from the UK Science and Technology Facilities Council (STFC). FM and SC acknowledge support from the Italian Ministry of University and Research (MUR), PRIN 2022 ‘EXSKALIBUR – Euclid-Cross-SKA: Likelihood Inference Building for Universe’s Research’, Grant No. 20222BBYB9, CUP D53D2300252 0006, from the Italian Ministry of Foreign Affairs and International Cooperation (MAECI), Grant No. ZA23GR03, and from the European Union – Next Generation EU. CC is supported by STFC grant ST/X000931/1. SLG and RM are supported by the South African Radio Astronomy Observatory and the National Research Foundation (grant no. 75415). SJ is supported by VIT Mauritius.

Code Availability Statement

CosmoWAP is publicly available at <https://github.com/craddis1/CosmoWAP> and the companion repository MATHWAP is available at <https://github.com/craddis1/MathWAP>. We also release a small tutorial notebook that recreates some of the results shown in this work. CosmoWAP is built on top of the public code `CLASS` [86, 87], and the following python packages and libraries: `NUMPY` [88], `SCIPY` [89], `MATPLOTLIB` [90], `CHAINCONSUMER` [91], `COBAYA` [80] and `COSMOPOWER` [81].

A Survey Details

We consider several different ongoing and future galaxy surveys, covering different tracers and redshift ranges, using redshift bins of constant width: a three-bin, 15,000 deg² DESI-like BGS ($0.05 < z < 0.6$), a five-bin, 15,000 deg² H α *Euclid*-like survey ($0.9 < z < 1.8$), a five-bin, 2000 deg² H α Roman-like survey ($0.5 < z < 2$), a ten-bin, Stage V 20,000 deg² MegaMapper-like Lyman-Break galaxy (LBG) survey over ($2 < z < 5$) as well as a ten-bin, futuristic Phase-2 SKA (SKAO2) 30,000 deg² HI galaxy survey over ($0.1 < z < 2$). For each tracer, we adopt an existing luminosity function from the literature, which we can use to calculate the evolution and magnification biases for a given flux or magnitude cut. The details of the luminosity function and the linear bias modelling for each survey is described below.

Euclid We adopt the ‘Model 3’ H α luminosity function [92, 93] and use a flux cut of $F_c = 2 \times 10^{-16}$ [erg cm⁻²s⁻¹]. In addition, we also adopt a model of linear bias, $b_1(x, z)$, as a function of redshift, z and luminosity x of [94] (Table 2). These fits derive from the semi-analytic galaxy formation GALFORM [95, 96]. The cumulative linear galaxy bias above a certain luminosity flux x_c is then given by

$$b_i(\geq x) = \frac{\int_{x_c}^{+\infty} dx b_i^h(x, z) \phi(x, z)}{\int dx \phi(x, z)} \quad (\text{A.1})$$

where $\phi(x, z)$ is the H α luminosity function.

Roman For the Roman-like H α survey our modelling is similar to the *Euclid*-like H α survey but instead we adopt the ‘Model’ 1 luminosity function from [92] with a flux cut of $F_s = 1 \times 10^{-16}$ [erg cm⁻²s⁻¹]. Our linear bias modelling is consistent with the H α model we use with the *Euclid*-like survey but with a different luminosity function.

MegaMapper We consider some idealised MegaMapper-like Lyman Break Galaxy (LBG) survey following [97], where we assume a UV Schechter luminosity function [98, 99] with an apparent magnitude cut, $m_c = 24.5$. For linear clustering bias, we adopt a redshift and apparent magnitude, m , dependent function also from [97],

$$b(z, m) = A(m)(1 + z) + B(m)(1 + z)^2 \quad (\text{A.2})$$

where $A(m) = -0.98(m - 25) + 0.11$ and $B(m) = 0.12(m - 25) + 0.17$. The bias model for the survey for a given apparent magnitude cut is then derived using Eq. (A.1).

BGS For the DESI-like BGS specifications, we assume a linear bias [1]

$$b_1(z) = 1.34/D(z), \quad (\text{A.3})$$

and we adopt the BGS luminosity functions detailed in [32] with an apparent magnitude cut, $m_c = 20$. This is a Schechter type luminosity function, using values from [100] with a K-correction following [101].

SKAO2 For the SKAO2 HI galaxy survey, we use a linear bias model from [102, 103]

$$b_1(z) = 0.554 e^{0.783z}. \quad (\text{A.4})$$

Expressions for evolution and magnification bias as well as the number density are interpolated from Table 2 in [32].

A.1 Bright-Faint Split

We consider a bright-faint split, as proposed by [39–41], whereby the single galaxy population is split according to luminosity into two independent samples. Defining a flux split, F_s , the faint sample then corresponds to the population of galaxies with an observed flux above the detector threshold, F_c , but below F_s while the bright catalogue just constitutes galaxies with an observed flux above F_s . Therefore, while treatment of the bright catalogue is relatively simple, as it can be considered as a regular survey with a flux cut at F_s , the faint catalogue biases depend on both the total and bright quantities.

For the faint populations, following [104], the linear bias, b_1^F , is given by

$$b_1^F = \frac{n^T b_1^T - n^B b_1^B}{n^F} \quad (\text{A.5a})$$

while following, [70, 105], the evolution, b_e^F , and magnification, \mathcal{Q}^F , biases can be expressed as

$$\mathcal{Q}^F = \frac{n^T}{n^T - n^B} \mathcal{Q}^B - \frac{n^B}{n^T - n^B} \mathcal{Q}^T \quad (\text{A.5b})$$

$$b_e^F = \frac{\partial \ln(n^T - n^B)}{\partial \ln(1 + z)}. \quad (\text{A.5c})$$

We consider bright-faint splits primarily for the *Euclid*-like H α and the MegaMapper-like LBG surveys, for which luminosity-dependent models of b_1 are available. Unless otherwise specified, we use splits of $F_s = 3 \times 10^{-16}$ [erg cm $^{-2}$ s $^{-1}$] and $m_s = 24$, respectively.

B Cross-Multipole Multi-Tracer Covariance

While it is common—and often advantageous—to compute the covariance from an ensemble of numerical simulations [e.g. 106], there are several motivations for analytic covariances in some cases. Indeed, on ultra-large scales one not only needs larger and more computationally expensive simulations, but one also needs to consider the impact of large-scale systematics, such as relativistic and wide-separation corrections. Here, therefore we calculate the analytic covariances to isolate and study each individual contribution to covariance. Including relativistic effects from a suite of simulations/mock will require them to include these effects, either through ray-tracing [e.g. 107, 108] or some other method, which is a non-trivial addition to the covariance pipeline.

The covariance for the even parity part of the power spectrum has been well studied [109–111]; however, while a few studies have considered the odd parity (multi-tracer) covariance [18, 60], these covariances are, in general, less well understood, and so here we provide a derivation for a full multipole analysis.

So for a given data vector in a specific redshift bin, we can express the full covariance matrix as a block matrix for each multipole pair

$$C^{PP} = \begin{pmatrix} C[P_{\ell_i}, P_{\ell_i}] & \dots & C[P_{\ell_i}, P_{\ell_n}] \\ \vdots & \ddots & \vdots \\ C[P_{\ell_n}, P_{\ell_i}] & \dots & C[P_{\ell_n}, P_{\ell_n}] \end{pmatrix}, \quad (\text{B.1})$$

where each cross/auto-multipole covariance block can then be written as a sub-matrix. For even-even multipoles, this is a 3×3 sub-matrix,

$$C(P_i, P_j) = \begin{pmatrix} C[P_{\ell_i}^{XX}, P_{\ell_j}^{XX}] & C[P_{\ell_i}^{XY}, P_{\ell_j}^{XX}] & C[P_{\ell_i}^{YY}, P_{\ell_j}^{XX}] \\ C[P_{\ell_i}^{XX}, P_{\ell_j}^{XY}] & C[P_{\ell_i}^{XY}, P_{\ell_j}^{XY}] & C[P_{\ell_i}^{YY}, P_{\ell_j}^{XY}] \\ C[P_{\ell_i}^{XX}, P_{\ell_j}^{YY}] & C[P_{\ell_i}^{XY}, P_{\ell_j}^{YY}] & C[P_{\ell_i}^{YY}, P_{\ell_j}^{YY}] \end{pmatrix} \quad (\text{B.2})$$

but in the odd-odd case, since we just consider the cross-power spectrum, we have

$$C(P_{i=\text{odd}}, P_{j=\text{odd}}) = C[P_{\ell_i}^{XY}, P_{\ell_j}^{XY}]. \quad (\text{B.3})$$

Odd-even and even-odd covariance matrices are therefore of shape 1×3 and 3×1 respectively, e.g.

$$C(P_i, P_{j=\text{odd}}) = \left(C[P_{\ell_i}^{XX}, P_{\ell_j}^{XY}] \ C[P_{\ell_i}^{XY}, P_{\ell_j}^{XY}] \ C[P_{\ell_i}^{YY}, P_{\ell_j}^{XY}] \right). \quad (\text{B.4})$$

See Fig. 9 for an overview of the full covariance for a given k -bin.

B.1 Covariance Matrix Element

Here, we compute the covariance of the multi-tracer power spectrum multipoles Yamamoto estimator, Eq. (2.3). As we are considering the covariance of complex variables, the covariance matrix element is defined with a conjugation

$$C[\hat{P}_{\ell_i}^{ab}, \hat{P}_{\ell_j}^{cd}](\mathbf{k}, \mathbf{q}) = \langle \hat{P}_{\ell_i}^{ab}(\mathbf{k}) \hat{P}_{\ell_j}^{cd}(\mathbf{q})^* \rangle. \quad (\text{B.5})$$

It is then useful to define the functions

$$F_{\ell_i}(\mathbf{k}) = \int_{\mathbf{x}} e^{-i\mathbf{k}\cdot\mathbf{x}} \mathcal{L}_{\ell_i}(\hat{\mathbf{k}} \cdot \hat{\mathbf{x}}) \Delta(\mathbf{x}), \quad (\text{B.6})$$

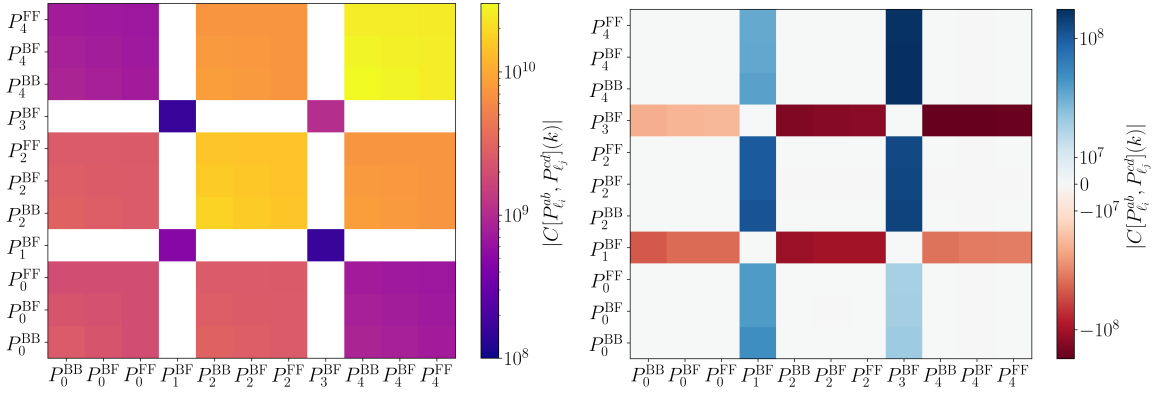


Figure 9: Real (left) and imaginary (right) parts of the full multipole covariance matrix for a multi-tracer analysis. We assume a bright-split of a *Euclid*-like survey with $F_s = 3 \times 10^{-16}$ [erg cm $^{-2}s^{-1}$], for a redshift bin, ($1 < z < 1.2$) and a k -bin centred at $k = 0.018$ [h/Mpc], including all effects except wide-separation, to the covariance.

such that, ignoring weights and windows, we can write the covariance element in terms of a Fourier space 4-point correlation function

$$C[P_{\ell_i}^{ab}, P_{\ell_j}^{cd}](\mathbf{k}, \mathbf{q}) = (2\ell_i + 1)(2\ell_j + 1) \int \frac{d\Omega_k}{4\pi} \int \frac{d\Omega_q}{4\pi} \left[\langle F_{\ell_i}^a(\mathbf{k}) F_0^b(-\mathbf{k}) F_{\ell_j}^c(\mathbf{q})^* F_0^d(-\mathbf{q})^* \rangle - \langle F_{\ell_i}^a(\mathbf{k}) F_0^b(-\mathbf{k}) \rangle \langle F_{\ell_j}^c(\mathbf{q})^* F_0^d(-\mathbf{q})^* \rangle \right]. \quad (\text{B.7})$$

Note that $F_{\ell_i}(-\mathbf{k}) = (-1)^{\ell_i} F_{\ell_i}(\mathbf{k})^*$.

Breaking the four-point function and assuming gaussianity (ignoring the connected trispectrum contribution), as well as assuming that the tracers are independent (e.g. see [112]), the covariance element simplifies to

$$C[P_{\ell_i}^{ab}, P_{\ell_j}^{cd}](\mathbf{k}, \mathbf{q}) = (2\ell_i + 1)(2\ell_j + 1) \int \frac{d\Omega_k}{4\pi} \int \frac{d\Omega_q}{4\pi} \left[\langle F_{\ell_i}^a(\mathbf{k}) F_{\ell_j}^c(\mathbf{q})^* \rangle \langle F_0^b(-\mathbf{k}) F_0^d(\mathbf{q}) \rangle + \langle F_{\ell_i}^a(\mathbf{k}) F_0^d(\mathbf{q}) \rangle \langle F_0^b(-\mathbf{k}) F_{\ell_j}^c(\mathbf{q})^* \rangle \right]. \quad (\text{B.8})$$

This is the full covariance element for our estimator, the full calculation including wide-separation corrections to this quantity is outlined in Section B.1.2, but, for simplicity and understanding, the plane-parallel constant redshift case is detailed below.

B.1.1 Plane-parallel Constant Redshift Limit

Assuming the plane parallel limit $\hat{\mathbf{d}} = d_z$, enables one to take the legendre outside the integral,

$$F_{\ell_i}^a(\mathbf{k}) = \mathcal{L}_i(\hat{\mathbf{k}} \cdot \hat{\mathbf{x}}) F_0^a(\mathbf{k}) \quad (\text{B.9})$$

and assuming the full plane-parallel constant redshift limit, such that the four points we are correlating have the same underlying statistics,

$$\begin{aligned} C[P_{\ell_i}^{ab}, P_{\ell_j}^{cd}](\mathbf{k}, \mathbf{q}) &= (2\ell_i + 1)(2\ell_j + 1) \int \frac{d\Omega_k}{4\pi} \int \frac{d\Omega_q}{4\pi} \mathcal{L}_i(\hat{\mathbf{k}} \cdot \hat{\mathbf{d}}) \mathcal{L}_j(\hat{\mathbf{q}} \cdot \hat{\mathbf{d}}) \\ &\times [\hat{P}^{ac}(\mathbf{k}, \mathbf{d}) \langle F_0^b(-\mathbf{k}) F_0^d(\mathbf{q}) \rangle \delta_D(\mathbf{k} - \mathbf{q}) + \hat{P}^{ad}(\mathbf{k}, \mathbf{d}) \langle F_0^b(-\mathbf{k}) F_0^c(-\mathbf{q}) \rangle \delta_D(\mathbf{k} + \mathbf{q})] \end{aligned} \quad (\text{B.10})$$

where the power spectrum includes shot noise contribution in the autocorrelation case assuming we have non-overlapping samples

$$\hat{P}^{ab}(\mathbf{k}, \mathbf{d}) = P_{\text{loc}}^{ab}(\mathbf{k}, \mathbf{d}) + \frac{\delta_{a,b}^K}{n_a}. \quad (\text{B.11})$$

where n_a is the number density of our given sample.

Simplifying this equation by switching an angular integral, as in Eq. (2.6), to an integral over \mathbf{q} and closing the Dirac deltas, leads to a general expression for each covariance element

$$C[P_{\ell_i}^{ab}, P_{\ell_j}^{cd}](k) = \frac{(2\ell_i + 1)(2\ell_j + 1)}{N_k} \int \frac{d\Omega_k}{4\pi} \mathcal{L}_i(\mu) [\mathcal{L}_j(\mu) \hat{P}^{ac}(k, \mu) \hat{P}^{bd}(k, \mu)^* \\ + \mathcal{L}_j(-\mu) \hat{P}^{ad}(k, \mu) \hat{P}^{bc}(k, \mu)^*]. \quad (\text{B.12})$$

Odd Multipole Covariance To examine the odd multipole covariance, we can split our density field into real (even), R , and imaginary (odd), I , parts, such that the local power spectrum can be expressed as (ignoring shot-noise)

$$P_{\text{loc}}^{ab}(k, \mu) = (R^a R^b + I^a I^b + i(I^a R^b - I^b R^a)) P(k), \quad (\text{B.13})$$

and therefore, using Eq. (B.12), one can see that the odd multipole diagonal covariance is proportional to

$$C[P_{\ell_i=\text{odd}}^{XY}, P_{\ell_j=\text{odd}}^{XY}](k) \propto (P^{XX} P^{YY} - P^{XY} P^{XY}), \quad (\text{B.14})$$

which can then be expressed in terms of the real and imaginary parts such that

$$C[P_{\ell_i=\text{odd}}^{XY}, P_{\ell_j=\text{odd}}^{XY}](k) \propto 2(R^X I^Y)^2 + 2(I^X R^Y)^2 - 4 R^X R^Y I^X I^Y \quad (\text{B.15})$$

This is simply the imaginary part of the power spectrum squared (as in [18]) and is zero if we neglect relativistic corrections. It is also even, real and always positive which is necessary for the covariance matrix to be positive semi-definite. The shot noise contribution to the covariance is also non-zero as it does not cancel because there is no shot-noise in the P^{XY} case. For odd-even components, the (off-diagonal) covariance is both odd and imaginary and $C[P_{\ell_i}^{XY}, P_{\ell_j}^{XY}](k) = C[P_{\ell_j}^{XY}, P_{\ell_i}^{XY}](k)^*$ which is necessary for the covariance matrix to be hermitian.

Relativistic Corrections to the Sample Variance As the integrated contributions to the power spectrum have a LOS dependence we need to include them in the full wide-separation framework (Appendix B.2), however we examine their impact on the sample variance with respect to the local relativistic contributions in this section. The integrated relativistic contributions to the monopole covariance are greater than the local relativistic contributions (see Fig. 10), and become relevant on large scales, just like the integrated contribution to the power spectrum itself. At higher redshifts the integrated effects are comparatively larger and indeed for MegaMapper the integrated contribution is greater than the Kaiser contribution for the largest scale k -bins where $k < 0.01 [h/\text{Mpc}]$.

B.1.2 Wide-Separation Corrections to the Covariance

Here, we calculate the wide-separations corrections to the covariance of the Yamamoto estimator. Following on from Eq. (B.8), the full multi-tracer gaussian multipole covariance can

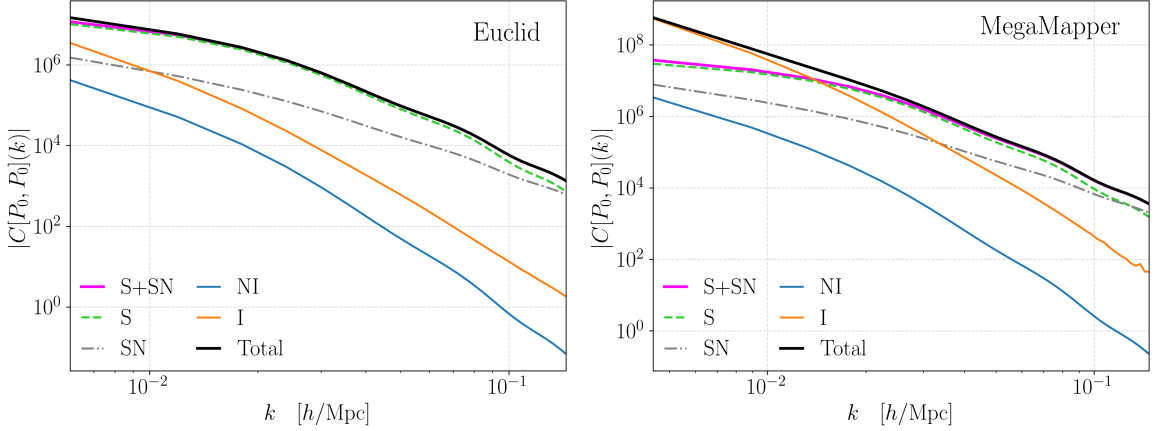


Figure 10: Contributions to the monopole covariance for a *Euclid*-like redshift bin ($1.26 < z < 1.44$) left and a *MegaMapper*-like redshift bin ($3.5 < z < 3.8$), where I represents all integrated contributions and SN is the shot-noise contribution. As we have cross-contributions in the covariance each additional corrections contains its mixing with the other contribution. So SN contains SN-S, the NI term contains the NI-S contribution and the NI-SN term and I contains I-S, I-SN and I-NI contributions. These are plotted over the same k -bins we use in our forecasts for this single redshift bin.

then be written, using Eq. (B.6), as

$$\begin{aligned} C[P_{\ell_i}^{ab}, P_{\ell_j}^{cd}](k) = & (2\ell_i + 1)(2\ell_j + 1) \int \frac{d\Omega_k}{4\pi} \frac{d\Omega_q}{4\pi} \int_{\mathbf{x}_1, \mathbf{x}_2, \mathbf{x}_3, \mathbf{x}_4} e^{-i\mathbf{k}\cdot\mathbf{x}_1} e^{i\mathbf{k}\cdot\mathbf{x}_3} \mathcal{L}_i(\hat{\mathbf{k}} \cdot \hat{\mathbf{x}}_1) \\ & \times \left[e^{i\mathbf{q}\cdot\mathbf{x}_2} e^{-i\mathbf{q}\cdot\mathbf{x}_4} \langle \Delta_g^a(\mathbf{x}_1) \Delta_g^c(\mathbf{x}_2) \rangle \langle \Delta_g^b(\mathbf{x}_3) \Delta_g^d(\mathbf{x}_4) \rangle \mathcal{L}_j(\hat{\mathbf{q}} \cdot \hat{\mathbf{x}}_2) \right. \\ & \left. + e^{-i\mathbf{q}\cdot\mathbf{x}_2} e^{i\mathbf{q}\cdot\mathbf{x}_4} \langle \Delta_g^a(\mathbf{x}_1) \Delta_g^d(\mathbf{x}_2) \rangle \langle \Delta_g^b(\mathbf{x}_3) \Delta_g^c(\mathbf{x}_4) \rangle \mathcal{L}_j(\hat{\mathbf{q}} \cdot \hat{\mathbf{x}}_4) \right]. \end{aligned} \quad (\text{B.16})$$

for the $t = 0$ Yamamoto estimator. If alternatively, we defined the covariance for the $t = 1$ estimator, then the \mathbf{x}_i dependence in the legendre polynomials change: $\mathcal{L}_i(\hat{\mathbf{k}} \cdot \hat{\mathbf{x}}_1) \rightarrow \mathcal{L}_i(\hat{\mathbf{k}} \cdot \hat{\mathbf{x}}_3)$ and $\mathcal{L}_j(\hat{\mathbf{k}} \cdot \hat{\mathbf{x}}_2) \leftrightarrow \mathcal{L}_j(\hat{\mathbf{k}} \cdot \hat{\mathbf{x}}_4)$. Our covariance is correlating the density field at 4 different points in the sky and under the assumption local statistical homogeneity, we can model this with one single LOS and as such our covariance is a function of a single k -vector. wide-separation corrections, then arise just as in the case of the power spectrum, from the breaking of this local statistical homogeneity, from RSD (wide-angle effects) and evolution of the signal with redshift (radial evolution effects). To calculate wide-separation effects the covariance we adopt the formalism developed in [51, 58].

It is then helpful to define our ‘local’ covariance

$$C[P_{\ell_i}^{ab}, P_{\ell_j}^{cd}](k) = \frac{1}{V_s} \int_{\mathbf{d}} C^{\text{loc}}[P_{\ell_i}^{ab}, P_{\ell_j}^{cd}](k; d), \quad (\text{B.17})$$

which is defined in a local region in which we perform our wide-separation series expansion in our 4-point function.

Defining a basis, in our local 4-point function as shown in Fig 11, with vectors $\mathbf{x}_{14}, \mathbf{x}_{24}, \mathbf{x}_{34}$ which simplifies the calculation for $\mathbf{d} = \mathbf{x}_4$ which is a natural choice for the LOS. The choice

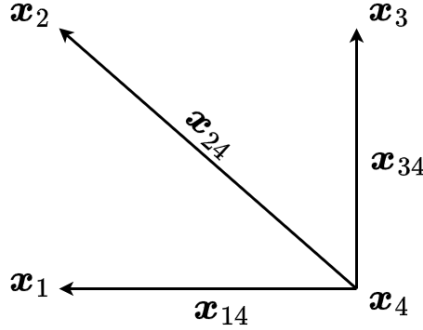


Figure 11: Position space local 4-point function. We define our basis with respect \mathbf{x}_4 which we pick as our LOS to simplify the calculations.

of LOS here is not too important; we do not ‘choose’ a LOS for our covariance like we do in our estimator (either endpoint). The choice of endpoint LOS in our estimator is already encoded in the covariance and as such the LOS choice only denotes the point at which we Taylor expand from to include wide-separation corrections.

Therefore, using $\mathbf{x}_{12} = \mathbf{x}_{14} - \mathbf{x}_{24}$, $\mathbf{x}_{23} = \mathbf{x}_{24} - \mathbf{x}_{34}$ and fixing $\mathbf{d} = \mathbf{x}_4$

$$\begin{aligned} C^{\text{loc}}[P_{\ell_i}^{ab}, P_{\ell_j}^{cd}](k; d) &= (2\ell_i + 1)(2\ell_j + 1) \int \frac{d\Omega_k}{4\pi} \frac{d\Omega_q}{4\pi} \int_{\mathbf{x}_{14}, \mathbf{x}_{24}, \mathbf{x}_{34}} e^{-i\mathbf{k}\cdot\mathbf{x}_{14}} e^{i\mathbf{k}\cdot\mathbf{x}_{34}} \mathcal{L}_i(\hat{\mathbf{k}} \cdot \hat{\mathbf{x}}_1) \\ &\quad \times \left[e^{i\mathbf{q}\cdot\mathbf{x}_{24}} \hat{\xi}_{\text{loc}}^{ac}(\mathbf{x}_1, \mathbf{x}_2) \hat{\xi}_{\text{loc}}^{bd}(\mathbf{x}_3, \mathbf{x}_4) \mathcal{L}_j(\hat{\mathbf{q}} \cdot \hat{\mathbf{x}}_2) \right. \\ &\quad \left. + e^{-i\mathbf{q}\cdot\mathbf{x}_{24}} \hat{\xi}_{\text{loc}}^{ad}(\mathbf{x}_1, \mathbf{x}_2) \hat{\xi}_{\text{loc}}^{bc}(\mathbf{x}_3, \mathbf{x}_4) \mathcal{L}_j(\hat{\mathbf{q}} \cdot \hat{\mathbf{x}}_4) \right] \end{aligned} \quad (\text{B.18})$$

where our local 2-point functions are defined, including shot-noise contributions (for simplicity and visualization we only compute wide-separation corrections on the non-integrated terms, though we could include the full local 2-point function as in Eq. (B.19)), by:

$$\hat{\xi}_{\text{loc}}^{ab}(\mathbf{x}_i, \mathbf{x}_j) = \int_{\mathbf{q}'} e^{i\mathbf{q}' \cdot \mathbf{x}_{ij}} \left[\mathcal{K}^a(\mathbf{q}', \mathbf{x}_i) \mathcal{K}^b(-\mathbf{q}', \mathbf{x}_j) P(\mathbf{q}') + \frac{\delta_{a,b}^K}{n_a} \right]. \quad (\text{B.19})$$

Now our next step is to reparameterise our kernels in terms of $\mathbf{d}, \mathbf{x}_{14}, \mathbf{x}_{24}, \mathbf{x}_{34}$ such that our endpoint vectors become

$$\mathbf{x}_i = \mathbf{d} + \mathbf{x}_{i4}, \quad (\text{B.20})$$

and the scalar magnitudes can be rewritten as

$$x_i = d \sqrt{1 + 2\mu_{i4}\epsilon_{i4} + \epsilon_{i4}^2}. \quad (\text{B.21})$$

Where $\mu_{i4} = \hat{\mathbf{x}}_{i4} \cdot \hat{\mathbf{d}}$ and we have defined our three expansion parameters, $\epsilon_i = x_{i4}/d$, for $i = 1, 2, 3$.

The approach is then to Taylor expand any $\mathbf{x}_1, \mathbf{x}_2, \mathbf{x}_3$ dependence in terms of $\epsilon_{14}, \epsilon_{24}, \epsilon_{34}$ respectively, about the point $\epsilon_{14} = \epsilon_{24} = \epsilon_{34} = 0$, to incorporate these corrections from the

breaking of statistical homogeneity in our local 4-point functions, Eq. (B.18). The ‘wide-angle’ part comes as we Taylor expand the unit vectors $\hat{\mathbf{x}}_i = \mathbf{d} + \mathbf{x}_{i4}/x_i$ while the ‘radial evolution’ part arises as we Taylor expand for any redshift dependent function (and therefore comoving distance dependent), $f(x_i)$.

Taylor expanding and truncating at some order, and expressing \mathbf{x}_{i4} in terms of their Cartesian vector components, we can then express our local 4-point as a sum over powers of our expansion parameters, $\epsilon_{14}, \epsilon_{24}, \epsilon_{34}$

$$\begin{aligned} C^{\text{loc}}[P_{\ell_i}^{ab}, P_{\ell_j}^{cd}](k; d) &= \frac{(2\ell_i + 1)(2\ell_j + 1)}{N_k} \int \frac{d\Omega_k}{4\pi} \int_{\mathbf{q}, \mathbf{x}_{14}, \mathbf{x}_{24}, \mathbf{x}_{34}, \mathbf{q}', \mathbf{k}'} e^{-i(\mathbf{k}-\mathbf{k}') \cdot \mathbf{x}_{14}} e^{i(\mathbf{k}+\mathbf{q}') \cdot \mathbf{x}_{34}} \\ &\quad \times \sum_{i_x, i_y, i_z} \epsilon_{14}^{(i_x+i_y+i_z)} \left[\left(\frac{x_{14,x}}{x_{14}} \right)^{i_x} \left(\frac{x_{14,y}}{x_{14}} \right)^{i_y} \left(\frac{x_{14,z}}{x_{14}} \right)^{i_z} \right] \\ &\quad \times \sum_{j_x, j_y, j_z} \epsilon_{24}^{(j_x+j_y+j_z)} \left[\left(\frac{x_{24,x}}{x_{24}} \right)^{j_x} \left(\frac{x_{24,y}}{x_{24}} \right)^{j_y} \left(\frac{x_{24,z}}{x_{24}} \right)^{j_z} \right] \\ &\quad \times \sum_{m_x, m_y, m_z} \epsilon_{34}^{(m_x+m_y+m_z)} \left[\left(\frac{x_{34,x}}{x_{34}} \right)^{m_x} \left(\frac{x_{34,y}}{x_{34}} \right)^{m_y} \left(\frac{x_{34,z}}{x_{34}} \right)^{m_z} \right] \\ &\quad \times \mathcal{C}_{i_x, i_y, i_z, j_x, j_y, j_z, m_x, m_y, m_z}^{a,b,c,d}(\mathbf{k}, \mathbf{q}, \mathbf{k}', \mathbf{q}', \mathbf{d}), \end{aligned} \tag{B.22}$$

where $\mathcal{C}_{i_x, i_y, i_z, j_x, j_y, j_z, m_x, m_y, m_z}^{a,b,c,d}$ is a coefficient that contains the \mathbf{k}, \mathbf{d} dependence of the covariance and reduces to

$$\begin{aligned} \mathcal{C}_{0, \dots, 0}^{a,b,c,d}(\mathbf{k}, \mathbf{q}, \mathbf{k}', \mathbf{q}', \mathbf{d}) &= \mathcal{K}^a(\mathbf{k}', \mathbf{d}) \mathcal{K}^b(\mathbf{q}', \mathbf{d}) P(\mathbf{k}') P(\mathbf{q}') \mathcal{L}_i(\hat{\mathbf{k}} \cdot \hat{\mathbf{d}}) \mathcal{L}_j(\hat{\mathbf{q}} \cdot \hat{\mathbf{d}}) \\ &\quad \times \left[\mathcal{K}^c(-\mathbf{k}', \mathbf{d}) \mathcal{K}^d(-\mathbf{q}', \mathbf{d}) e^{-i(\mathbf{k}'-\mathbf{q}) \cdot \mathbf{x}_{24}} + \mathcal{K}^d(-\mathbf{k}', \mathbf{d}) \mathcal{K}^c(-\mathbf{q}', \mathbf{d}) e^{-i(\mathbf{k}'+\mathbf{q}) \cdot \mathbf{x}_{24}} \right] \\ &\quad + \mathcal{L}_i(\hat{\mathbf{k}} \cdot \hat{\mathbf{d}}) \mathcal{L}_j(\hat{\mathbf{q}} \cdot \hat{\mathbf{d}}) \left[\right. \\ &\quad \left. e^{-i(\mathbf{k}'-\mathbf{q}) \cdot \mathbf{x}_{24}} \left(\frac{\delta_{a,c}^K}{n_a} \mathcal{K}^b(\mathbf{q}', \mathbf{d}) \mathcal{K}^d(-\mathbf{q}', \mathbf{d}) P(\mathbf{q}') + \frac{\delta_{b,d}^K}{n_b} \mathcal{K}^a(\mathbf{k}', \mathbf{d}) \mathcal{K}^c(-\mathbf{k}', \mathbf{d}) P(\mathbf{k}') \right) \right. \\ &\quad \left. + e^{-i(\mathbf{k}'+\mathbf{q}) \cdot \mathbf{x}_{24}} \left(\frac{\delta_{a,d}^K}{n_a} \mathcal{K}^b(\mathbf{q}', \mathbf{d}) \mathcal{K}^c(-\mathbf{q}', \mathbf{d}) P(\mathbf{q}') + \frac{\delta_{b,c}^K}{n_b} \mathcal{K}^a(\mathbf{k}', \mathbf{d}) \mathcal{K}^d(-\mathbf{k}', \mathbf{d}) P(\mathbf{k}') \right) \right. \\ &\quad \left. + \left(e^{-i(\mathbf{k}'-\mathbf{q}) \cdot \mathbf{x}_{24}} \frac{\delta_{a,c}^K}{n_a} \frac{\delta_{b,d}^K}{n_b} + e^{-i(\mathbf{k}'+\mathbf{q}) \cdot \mathbf{x}_{24}} \frac{\delta_{a,d}^K}{n_a} \frac{\delta_{b,c}^K}{n_b} \right) \right], \end{aligned} \tag{B.23}$$

at zeroth-order (in the plane-parallel constant redshift limit). The second square bracket here includes the shot-noise contribution to the covariance. In this case, we get back Eq. (B.12).

However, to compute the full covariance we then use the Fourier relation,

$$\frac{\partial}{\partial k_j} F(\mathbf{k}) = -i \int d^3 \mathbf{x} e^{-i \mathbf{k} \cdot \mathbf{x}} x_j f(\mathbf{x}), \tag{B.24}$$

such that we can remove the $x_{i4,j}$ dependence from inside the integral as $x_{14,j} \rightarrow i\partial_{(k-k')_j}$, $x_{34,j} \rightarrow -i\partial_{(k+q')_j}$ and then $x_{24,j} \rightarrow i\partial_{(k\pm q)_j}$, where the \pm depends on which \mathbf{x}_{24} exponential

is being considered. Once there is no \mathbf{x}_{i4} dependence left in the real space integrals, we form Dirac deltas ($\delta_D(\mathbf{k} - \mathbf{k}')$, $\delta_D(\mathbf{k} + \mathbf{q}')$, $\delta_D(\mathbf{k} \pm \mathbf{q})$) from the \mathbf{x}_{i4} integrals which close the \mathbf{k}' , \mathbf{k}' , \mathbf{q} integrals, such that the covariance is dependent on a single k -magnitude. Therefore the local covariance can be expressed such that there are n partial derivatives acting on each coefficient for each term in the series

$$C^{\text{loc}}[P_{\ell_i}^{ab}, P_{\ell_j}^{cd}](k; d) = \sum_n \left(\frac{1}{d} \right)^n \sum_{i_x, i_y, i_z, j_x, j_y, j_z, m_x, m_y, m_z}^{i_x + i_y + i_z + j_x + j_y + j_z + m_x + m_y + m_z = n} \left(\partial_{k_x}^{i_x + j_x + m_z} \partial_{k_y}^{i_y + j_y + m_y} \partial_{k_z}^{i_z + j_z + m_z} \right) \times (-1)^{j_x + j_y + j_z} C_{i_x, i_y, i_z, j_x, j_y, j_z, m_x, m_y, m_z}(\mathbf{k}, \pm \mathbf{k}, \mathbf{k}, \mathbf{d}). \quad (\text{B.25})$$

The full covariance with wide-separation corrections is then given by averaging over the survey as in Eq. (B.17).

We truncate this expansion at $n = 2$ for simplicity in our analysis. While these corrections are unimportant to the even multipoles, they do make a significant impact to the odd multipole covariance, Fig. 12. For the odd multipoles there is no pure Kaiser contribution, instead the leading contribution for the *Euclid* and MegaMapper-like samples is shot-noise. On large scales, the wide-separation, particularly the radial evolution, corrections to the dipole covariance become non-negligible. Notably, for the surveys considered here, these are larger than the contribution from the imaginary part of the power spectrum (Appendix B.1.1). Therefore, wide-separation corrections to the odd multipole covariance for a multi-tracer analysis should be considered in future analyses, especially for samples with high number densities. Though generally, the wide-angle corrections will naturally be included if one computes the covariance from a suite of simulations, the radial evolution corrections requires simulations that have the correct non-discrete redshift evolution.

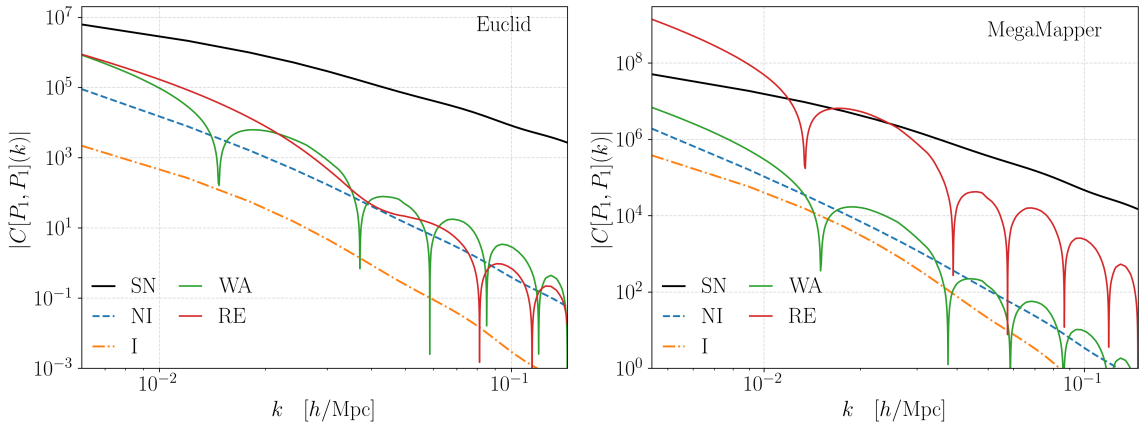


Figure 12: Contributions to the bright-faint dipole covariance for a *Euclid*-like redshift bin ($1.26 < z < 1.44$) left and a MegaMapper-like redshift bin ($3.5 < z < 3.8$), where I represents all integrated contributions and SN is the shot-noise contribution. The wide-angle term (WA) is represented in green and the radial evolution term (RE) is represented in red. These are plotted over the same k -bins we use in our forecasts for this single redshift bin.

B.2 Integrated Contributions to the Covariance

Due to the LOS dependence of the integrated contributions, we need to define with respect to our LOS choice, $\mathbf{d} = \mathbf{x}_4$. In this case, this is equivalent to computing integrated power spectrum with $t = 1$. We outline this for the I×I contribution below.

The integrated contribution to the local 2-point function (this is an additional term to Eq. (B.19)) can be written as,

$$\hat{\xi}_{\text{loc}}^{ab, \text{I}\times\text{I}}(\mathbf{x}_i, \mathbf{x}_j) = \int_0^1 dy_i \int_0^1 dy_j \int_{\mathbf{q}'} e^{i\mathbf{q}' \cdot \mathbf{r}_{ij}} \left[x_i x_j \mathcal{K}^a(\mathbf{q}', \mathbf{x}_i, r) \mathcal{K}^b(-\mathbf{q}', \mathbf{x}_j, r) P(\mathbf{q}') \right], \quad (\text{B.26})$$

and then re-expressing the exponential using $\mathbf{x}_i = \mathbf{d} + \mathbf{x}_{i4}$

$$\begin{aligned} \hat{\xi}_{\text{loc}}^{ab, \text{I}\times\text{I}}(\mathbf{x}_i, \mathbf{x}_j) &= \int_0^1 dy_i \int_0^1 dy_j \int_{\mathbf{q}'} e^{i y_i \mathbf{q}' \cdot \mathbf{x}_{i4}} e^{-i y_j \mathbf{q}' \cdot \mathbf{x}_{j4}} e^{i(y_i - y_j) \mathbf{q}' \cdot \mathbf{d}} \\ &\quad \times x_i x_j \mathcal{K}^a(\mathbf{q}', \mathbf{x}_i, r) \mathcal{K}^b(-\mathbf{q}', \mathbf{x}_j, r) P(\mathbf{q}'). \end{aligned} \quad (\text{B.27})$$

Therefore, substituting these expressions into Eq. (B.18) we can see we will end up with the Dirac-deltas ($\delta_D(\mathbf{k} - y_1 \mathbf{k}')$, $\delta_D(\mathbf{k} + y_3 \mathbf{q}')$, $\delta_D(y_2/y_1 \mathbf{k} \pm \mathbf{q})$). As the only \mathbf{q} dependence is contained in a unit vector in the legendre polynomial this last y_2/y_1 factor is unimportant and we can compute the integrated contributions in the usual way. Conveniently, this then corresponds to $t = 1$ case, such that we can write an example integrated contribution to the covariance as

$$\begin{aligned} C[P_{\ell_i}^{ab, \text{I}\times\text{I}}, P_{\ell_j}^{cd}](k) &= \frac{(2\ell_i + 1)(2\ell_j + 1)}{N_k} \int \frac{d\Omega_k}{4\pi} \mathcal{L}_i(\mu) [\mathcal{L}_j(\mu) \hat{P}_{t=1}^{ac, \text{I}\times\text{S}}(k, \mu) \hat{P}_{t=1}^{bd, \text{S}\times\text{I}}(k, \mu)^* \\ &\quad + \mathcal{L}_j(-\mu) \hat{P}_{t=1}^{ad, \text{I}\times\text{S}}(k, \mu) \hat{P}_{t=1}^{bc, \text{S}\times\text{I}}(k, \mu)^*], \end{aligned} \quad (\text{B.28})$$

for the zeroth order term of the wide-separation expansion.

C Integrated × Local Contribution to the Local Power Spectrum

Here we give a brief summary of the mixing contribution between the integrated and local terms in power spectrum, which has also been calculated in [31, 51]. The I×S contribution to the local 2-point correlation, from the expansion in Eq. (2.13), is composed of 2 asymmetric cross-terms

$$\begin{aligned} \xi_{\text{loc}}(\mathbf{x}_1, \mathbf{x}_2) &= \int_{\mathbf{q}} \left[\int_0^{x_1} dr_1 e^{i\mathbf{q} \cdot (\mathbf{r}_1 - \mathbf{x}_2)} \mathcal{K}^{\text{I}}(\mathbf{q}, \mathbf{x}_1, r_1) \mathcal{K}(-\mathbf{q}, \mathbf{x}_2) \right. \\ &\quad \left. + \int_0^{x_2} dr_2 e^{i\mathbf{q} \cdot (\mathbf{x}_1 - \mathbf{r}_2)} \mathcal{K}(\mathbf{q}, \mathbf{x}_1) \mathcal{K}^{\text{I}}(-\mathbf{q}, \mathbf{x}_2, r_2) \right] P(q) \end{aligned} \quad (\text{C.1})$$

with two integrals separate 1D integrals, where $\mathcal{K}(\mathbf{q}, \mathbf{x})$ represents any combination of the local kernels – though we still refer to this as the I×S term.

Then as with the I×I case, we can rearrange the exponentials, $\mathbf{r}_1 = \frac{r_1}{x_1} \mathbf{x}_1$, $\mathbf{r}_2 = \frac{r_2}{x_2} \mathbf{x}_2$ and $\mathbf{x}_1 = \mathbf{d} + t\mathbf{x}_{12}$, $\mathbf{x}_2 = \mathbf{d} - (1-t)\mathbf{x}_{12}$, such that

$$e^{i\mathbf{q} \cdot (\mathbf{r}_1 - \mathbf{x}_2)} = e^{i(\frac{r_1}{x_1} - 1)(\mathbf{q} \cdot \mathbf{d})} e^{i(\frac{r_1}{x_1} t + (1-t))(\mathbf{q} \cdot \mathbf{x}_{12})} \quad (\text{C.2a})$$

$$e^{i\mathbf{q} \cdot (\mathbf{x}_1 - \mathbf{r}_2)} = e^{i(1 - \frac{r_2}{x_2})(\mathbf{q} \cdot \mathbf{d})} e^{i(t + (1-t)\frac{r_2}{x_2})(\mathbf{q} \cdot \mathbf{x}_{12})}. \quad (\text{C.2b})$$

Taking the zeroth order term in our perturbative wide-separation corrections, and again redefining the integration variables $y_1 = r_1/x_1$, $y_2 = r_2/x_2$, the I×S contribution to the local power spectrum can be written as

$$P_{\text{loc}}^{\text{I} \times \text{S}}(\mathbf{k}; \mathbf{d}) = \int_{\mathbf{q}, \mathbf{x}_{12}} \left[\int_0^1 dy_1 e^{i(y_1-1)(\mathbf{q} \cdot \mathbf{d})} e^{-i(\mathbf{k} - (1+t(y_1-1))\mathbf{q}) \cdot \mathbf{x}_{12}} d\mathcal{K}^{\text{I}}(\mathbf{q}, \mathbf{d}, d y_1) \mathcal{K}(-\mathbf{q}, \mathbf{d}) \right. \\ \left. + \int_0^1 dy_2 e^{i(1-y_2)(\mathbf{q} \cdot \mathbf{d})} e^{-i(\mathbf{k} - (y_2+t(1-y_2))\mathbf{q}) \cdot \mathbf{x}_{12}} d\mathcal{K}(\mathbf{q}, \mathbf{d}) \mathcal{K}^{\text{I}}(-\mathbf{q}, \mathbf{d}, d y_2) \right] P(q), \quad (\text{C.3})$$

Then, as there is now no \mathbf{x}_{12} dependence left in the kernels, the \mathbf{x}_{12} integral therefore becomes a Dirac-delta. Using the shifting property of the Dirac-delta and defining two functions $G_1(y_1) = (1 + t(y_1 - 1))$ and $G_2(y_2) = (y_2 + t(1 - y_2))$, we can then simplify such that

$$P_{\text{loc}}^{\text{I} \times \text{S}}(k, \mu; d) = \int_0^1 dy_1 e^{i(y_1-1)k \mu d/G_1(y_1)} dG_1(y_1)^{-3} \mathcal{K}^{\text{I}}(G_1(y_1)^{-1}k, \mu, d, y_1) \\ \times \mathcal{K}(G_1(y_1)^{-1}k, -\mu) P(G_1(y_1)^{-1}k) \\ + \int_0^1 dy_2 e^{i(1-y_2)k \mu d/G_2(y_2)} dG_2(y_2)^{-3} \mathcal{K}^{\text{I}}(G_2(y_2)^{-1}k, -\mu, d, y_2) \\ \times \mathcal{K}(G_2(y_2)^{-1}k, \mu) P(G_2(y_2)^{-1}k). \quad (\text{C.4})$$

The numerical computation of these integrals is discussed in [Appendix G](#).

D Local Kernels

The linear standard ‘Newtonian’ Kaiser kernel is given by

$$\mathcal{K}_{\text{N}}(\mathbf{q}, \mathbf{x}) = D [b_1 + f(\hat{\mathbf{q}} \cdot \hat{\mathbf{x}})^2], \quad (\text{D.1})$$

and the linear local relativistic correction is given by

$$\mathcal{K}_{\text{NI}}(\mathbf{q}, \mathbf{x}) = D \left[i(\mathbf{q} \cdot \hat{\mathbf{x}}) \frac{\gamma_1}{q_1^2} + \frac{\gamma_2}{q_1^2} \right] \quad (\text{D.2})$$

where γ_1 and γ_2 contain the redshift dependence of the projection effects such that

$$\frac{\gamma_1}{\mathcal{H}} = D f \left[b_e - 2\mathcal{Q} - \frac{2(1-\mathcal{Q})}{x_1 \mathcal{H}} - \frac{-(1+z)\mathcal{H}_z}{\mathcal{H}^2} \right], \quad (\text{D.3a})$$

$$\frac{\gamma_2}{\mathcal{H}^2} = D f(3 - b_e) + \frac{3}{2} D \Omega_m \left[2 + b_e - f - 4\mathcal{Q} - \frac{2(1-\mathcal{Q})}{x_1 \mathcal{H}} - \frac{-(1+z)\mathcal{H}_z}{\mathcal{H}^2} \right]. \quad (\text{D.3b})$$

As previously, we drop the explicit comoving distance (redshift) dependence in the kernels. The local type PNG kernel can be expressed as

$$\mathcal{K}_{\text{NG}}(k, x) = D b_\phi / \mathcal{M}(k) \quad (\text{D.4})$$

where \mathcal{M} is the scaling factor between the primordial scalar power spectrum and the late-time matter power spectrum and the non-gaussian bias b_ϕ is given, assuming the universality relation, by

$$b_\phi = 2 \delta_c f_{\text{NL}} (b_1 - 1) \quad (\text{D.5})$$

and we assume $\delta_c = 1.686$, the critical density for spherical collapse.

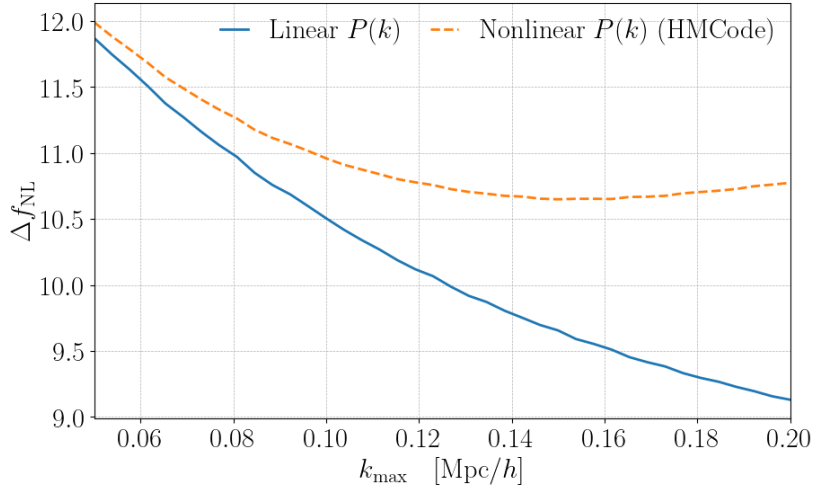


Figure 13: Forecasted bias from neglecting solely integrated (I×S and I×I) for a *Euclid*-like analysis, for varying k_{\max} , on the best fit measurement of f_{NL} . For the dashed line we use the non-linear power spectrum instead of the linear power spectrum in the forecast.

E Bias from Non-linear Contributions to the Integrated Effects

To quantify the impact of non-linear effects, Section 4.1.1, in our typical f_{NL} analysis, Fig. 13 shows effect of this simple non-linear modelling on the bias on local type f_{NL} from neglecting purely integrated effects (here we also use the non-linear power spectrum from the covariances). We can see compared to the linear case, there is an increase to the bias that increases with k_{\max} . Even though there is relatively modest constraining power on f_{NL} at these small scales, we can see that the large increase in the amplitude of the integrated effects at these scales causes the bias on the measurement of f_{NL} to increase.

In our forecasts, we also neglect the impact of fingers of god damping, however we note this can be trivially added to our pipeline; though it would have relatively small impact on the forecasts considered here due to our focus on large scale effects.

F LOS Dependence of the Local Power Spectrum

Here, we reiterate the key points on the properties of the local power spectrum, and in particular the integrated contributions to it, on large scales:

1. Contributions that break translation invariance in our local power spectrum are t -dependent; these are both consequences of \mathbf{d} -dependence in the local power spectrum.
2. At zeroth order in our wide-separation x_{12}/d expansion, local contributions to the local power spectrum are translation invariant; however, outside the Limber approximation, the integrated effects break translation invariance. Consequently, the non-diagonal parts (which are neglected in a Limber-type approximation) of the I×I term (and the non source-source correlation for the I×S term) can be considered a wide-separation type effect—analogous to the non-zeroth order terms in the x_{12}/d expansion.
3. These wide-separation type corrections to the local power spectrum depend on the choice of LOS (they are t -dependent), and one can therefore observe their relevance by

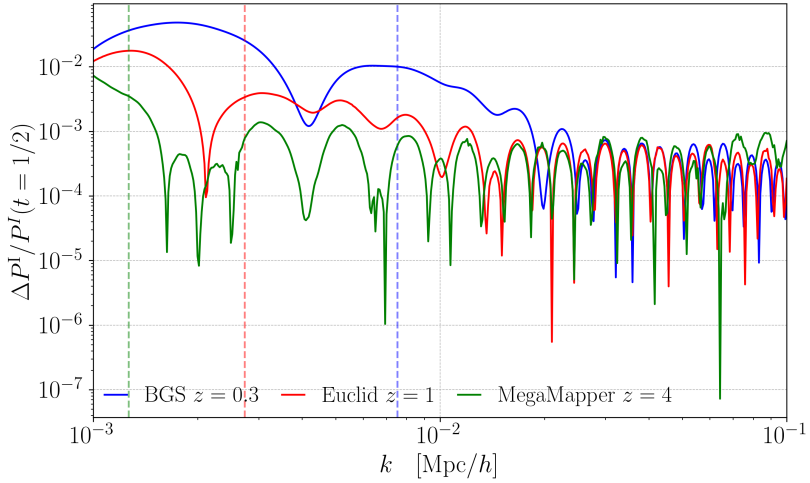


Figure 14: Fractional difference of the $I \times I$ contribution to the power spectrum monopole between $t = 1/2$ and $t = 0$, for three different surveys specifications. The dashed vertical lines represent the scale which corresponds to a separation such that $x_{12}/d = 1$, for each survey. Thus, as we approach these scales, we expect the wide-separation expansion to break down.

examining the t -dependence in the monopole of the local power spectrum (Fig. 14). In general, they scale as $(1/k d)^n$, behaving similarly to the local wide-separation terms.

4. Thus, outside both the Limber approximation and the plane-parallel, constant redshift limit, we have a t -dependent integrated local power spectrum. However, when one averages over the survey volume, the power spectrum monopole becomes independent of the LOS choice⁸ in the local 2-point function, as expected when considering the Yamamoto estimator. For higher multipoles, this is no longer the case due to the additional LOS dependence introduced when decomposing the multipoles.

F.1 Mixing in the Integrated terms beyond the Limber approximation

As the off-diagonal parts of the integrand correlate two different redshifts, this breaks the $y_1 \leftrightarrow y_2$ symmetry and thus the integrated contribution is dependent on the LOS choice even in the plane-parallel constant redshift limit. Therefore, these terms are dependent on the LOS choice in our estimator. We can view this effect as mixing the multipoles for different choices of t .

If we return to Eq. (2.20), we can express the $I \times I$ contribution as

$$P_{\text{loc}}^{I \times I}(k, \mu, d; t) = \int_0^1 dy_1 \int_0^1 dy_2 e^{i \mu A_t(y_1, y_2)} \mathcal{F}\left(\frac{k}{G_t}, \mu; d, y_1, y_2\right), \quad (\text{F.1})$$

where

$$G_t(y_1, y_2) \equiv y_2 + t(y_1 - y_2), \quad A_t(y_1, y_2) \equiv (y_1 - y_2) \frac{k d}{G_t(y_1, y_2)}, \quad (\text{F.2})$$

⁸While this may initially appear unconvincing, if one considers a correlation function that is simply a polynomial in \mathbf{x}_1 and \mathbf{x}_2 (e.g., $\xi(x_1, x_2) = x_1^2 x_2^2$, which has a finite expansion in x_{12}/d), one can see that the survey-averaged monopole is independent of t . This can be computed via pair counting: for each pair, the comoving distance d at which we evaluate the pair is affected by our LOS choice. For an endpoint LOS, one samples slightly more extremal values of d than in the midpoint case.

and \mathcal{F} denotes the remaining (non-exponential) factor

$$\mathcal{F}\left(\frac{k}{G_t}, \mu; d, y_1, y_2\right) \equiv d^2 G_t^{-3} \mathcal{K}^I\left(\frac{k}{G_t}, \mu, d, y_1\right) \mathcal{K}^I\left(\frac{k}{G_t}, -\mu, d, y_2\right) P\left(\frac{k}{G_t}\right).$$

The key point is that the t -dependence appears in *both* the oscillatory factor $e^{i\mu A_t}$ and in the rescaling $k \rightarrow k/G_t$ inside \mathcal{F} . This changes the full μ -dependence of the integrand, so projecting onto Legendre multipoles necessarily mixes different ℓ .

A simple way to see the mixing is to expand the oscillatory factor in Legendre polynomials,

$$e^{i\mu A} = \sum_{n=0}^{\infty} (2n+1) i^n j_n(A) \mathcal{L}_n(\mu), \quad (\text{F.3})$$

and (for fixed y_1, y_2) expand the remaining μ -dependence as

$$\mathcal{F}\left(\frac{k}{G_t}, \mu; d, y_1, y_2\right) = \sum_{\ell'} \mathcal{F}_{\ell'}\left(\frac{k}{G_t}; d, y_1, y_2\right) \mathcal{L}_{\ell'}(\mu). \quad (\text{F.4})$$

Then the local multipoles are

$$P_{\ell, \text{loc}}^{\text{I}\times\text{I}}(k, d; t) = \frac{2\ell+1}{2} \int_{-1}^1 d\mu P_{\text{loc}}^{\text{I}\times\text{I}}(k, \mu, d; t) \mathcal{L}_{\ell}(\mu), \quad (\text{F.5})$$

and inserting Eq. (F.1)–Eq. (F.3) gives the schematic coupling

$$P_{\ell, \text{loc}}^{\text{I}\times\text{I}}(k, d; t) = \int_0^1 dy_1 \int_0^1 dy_2 \sum_{\ell', n} \mathcal{M}_{\ell\ell'n}[A_t(y_1, y_2)] \mathcal{F}_{\ell'}\left(\frac{k}{G_t}; d, y_1, y_2\right), \quad (\text{F.6})$$

with mixing coefficients

$$\mathcal{M}_{\ell\ell'n}(A) \equiv (2n+1) i^n j_n(A) \frac{2\ell+1}{2} \int_{-1}^1 d\mu \mathcal{L}_{\ell}(\mu) \mathcal{L}_{\ell'}(\mu) \mathcal{L}_n(\mu). \quad (\text{F.7})$$

The triple-Legendre integral in Eq. (F.7) enforces the usual selection rules (triangle conditions and $\ell + \ell' + n$ even), so the monopole at a given t generically receives contributions from multiple even ℓ' once $n \geq 2$ is present. Since A_t (and k/G_t) depends on t , the weights multiplying each ℓ' differ between $t = 0$ and $t = 1/2$.

This implies a non-trivial linear relation of the form

$$P_{\ell, \text{loc}}^{\text{I}\times\text{I}}(k, d; t=0) = \sum_{\ell'} T_{\ell\ell'}(k, d) P_{\ell', \text{loc}}^{\text{I}\times\text{I}}(k, d; t=\tfrac{1}{2}), \quad (\text{F.8})$$

where $T_{\ell\ell'}$ is induced by Eq. (F.6)–Eq. (F.7) and the t -dependence of G_t and A_t , and is given by

$$\begin{aligned} T_{\ell\ell'}(A_0, A_{1/2}) &= \frac{2\ell+1}{2} \int_{-1}^1 d\mu \mathcal{L}_{\ell}(\mu) \mathcal{L}_{\ell'}(\mu) \exp[i\mu(A_0 - A_{1/2})] \\ &= (2\ell+1) \sum_n (2n+1) i^n j_n(A_0 - A_{1/2}) \binom{\ell \ \ell' \ n}{0 \ 0 \ 0}^2. \end{aligned} \quad (\text{F.9})$$

In particular the monopole at $t = 0$ contains (in general) pieces that would project onto $\ell' = 2, 4, \dots$ at $t = 1/2$, and vice versa. Note that the non-integrated limit is equivalent to $A=0$ which implies $n = 0$ and $\ell' = \ell$.⁹

Finally, the special role of $t = \frac{1}{2}$ is that for single-tracer auto-correlations the $I \times I$ integrand has a $y_1 \leftrightarrow y_2$ symmetry which makes the local power spectrum even in μ at leading order (so odd multipoles vanish), whereas this symmetry is broken for endpoint choices (e.g. $t = 0$ where $G_t = y_2$), allowing an odd/imaginary part to appear. This is the same origin as the t -dependent odd-parity signal discussed in [Section 2.2.1](#): it is a wide-separation type effect caused by the breaking of local translation invariance by the integrated contributions, rather than by the usual polynomial μ -structure of the local terms.

G Properties of the Integrands

The $I \times S$ term, [Appendix C](#), is computed by a oscillatory 1D integrand, [Fig. 15](#), and, ignoring the μ dependence in the kernels, has the general form of $\text{sinc}(k \frac{r-d}{d+r})$, weighted by the r dependence in the integrated kernels. Therefore, as this behaves like a sine integral, the $I \times S$ term is largely determined by its behaviour close to the source as the correlation of the source density fields with the density fields along the path largely cancel. Therefore, the value of the integral, for a fixed comoving distance d , is dependent of the frequency of the sine wave, set by the k scale; thus one can see that this produces the characteristic wiggles in the $I \times S$ contribution when plotted as a function of k , [Fig. 2](#).

Alternatively, one can consider the $I \times S$, [Eq. \(C.4\)](#) (or $I \times I$ - [Eq. \(2.20\)](#)) contribution as a Fourier transform over y (y_1 and y_2) with a sharp window function at the source and observer. Therefore, the wiggles are a Gibbs phenomenon due to sharp cut-off in the integrand.

These oscillations in k are damped in the lensing contribution, as the real part of the lensing kernel peaks halfway between the observer and source, due to the $(d-r)(d)$ dependence, and therefore the sharp cut-offs are partially smoothed. The imaginary part however

⁹Starting from [Eq. \(2.20\)](#), compare the endpoint and midpoint choices by factorising the phase in the integrand,

$$e^{i\mu A_0(y_1, y_2)} = e^{i\mu A_{1/2}(y_1, y_2)} e^{i\mu \Delta A(y_1, y_2)}, \quad \Delta A \equiv A_0 - A_{1/2}, \quad (\text{F.10})$$

where A_t is defined below [Eq. \(2.20\)](#). Inserting [Eq. \(F.10\)](#) into [Eq. \(2.20\)](#), and using the plane-wave/Legendre expansion [Eq. \(F.3\)](#) for the midpoint factor,

$$e^{i\mu A_{1/2}} = \sum_{n=0}^{\infty} (2n+1) i^n j_n(A_{1/2}) \mathcal{L}_n(\mu), \quad (\text{F.11})$$

together with a Legendre expansion of the remaining bracket

$$e^{i\mu \Delta A} \mathcal{F}_0(\mu) = \sum_{\ell'} \left[e^{i\mu \Delta A} \mathcal{F}_0 \right]_{\ell'} \mathcal{L}_{\ell'}(\mu), \quad (\text{F.12})$$

(where \mathcal{F}_0 denotes the non-exponential part of the $t = 0$ integrand in [Eq. \(2.20\)](#)), the multipole projection gives a coupled sum over ℓ' and n involving the Gaunt integral [Eq. \(F.7\)](#). This yields the mixing kernel

$$P_{\ell, \text{loc}}^{I \times I}(k, d; 0) = \int_0^1 dy_1 \int_0^1 dy_2 \sum_{\ell'} T_{\ell\ell'}(A_{1/2}(y_1, y_2)) \left[e^{i\mu \Delta A} \mathcal{F}_0 \right]_{\ell'}(k, d; y_1, y_2), \quad (\text{F.13})$$

with

$$T_{\ell\ell'}(A) \equiv (2\ell + 1) \sum_{n=0}^{\infty} (2n+1) i^n j_n(A) \begin{pmatrix} \ell & \ell' & n \\ 0 & 0 & 0 \end{pmatrix}^2. \quad (\text{F.14})$$

For non-integrated local terms there is no t -dependent phase analogous to A_t in [Eq. \(2.20\)](#) (so effectively $\Delta A = 0$); since $j_n(0) = \delta_{n0}$, [Eq. \(F.14\)](#) reduces to $T_{\ell\ell'} = \delta_{\ell\ell'}$, i.e. no multipole mixing.

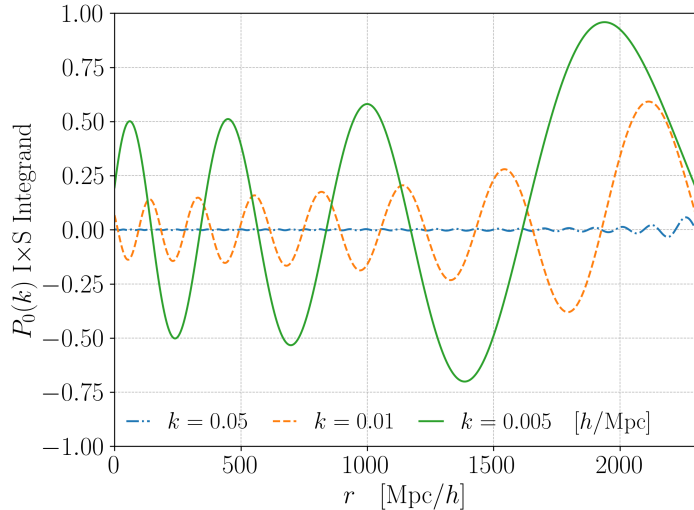


Figure 15: Integrand of the $I \times S$ term from observer to source at $z = 1$ for a *Euclid*-like H α survey for a few different k -values, for $t = 1/2$.

just has a $(d - r)$ dependence and therefore has a sharp cut-off at the observer. Furthermore, as the lensing kernel is comparatively small close to the source, this therefore reduces the relative size of the lensing contribution to the $I \times S$ term.

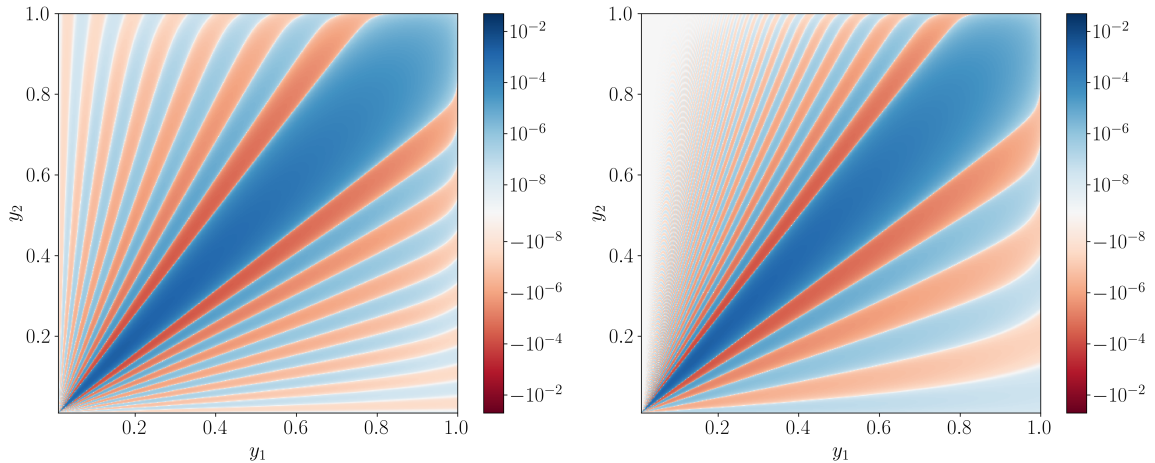


Figure 16: Real single tracer integrand of the monopole for the $I \times I$ contribution with $t = 1/2$ (left) and $t = 0$ (right) for a *Euclid*-like H α survey for $k = 0.01$ at $z = 1.5$. Bottom left corner, $y_1 = y_2 = 0$, represents the observer and top right, $y_1 = y_2 = 1$, represents the source.

The single tracer 2D $I \times I$ integrand, Fig. 16, is symmetric (anti-symmetric) for the even (odd) multipoles about $y_1 = y_2$ for $t = 1/2$ but this symmetry is broken for other LOS choices. This, therefore generates the imaginary dipole signal for an endpoint LOS as in the Yamamoto estimator, Eq. (2.3). Similarly, for the $I \times S$ term, the two integrals (IS and SI) only cancel in the single tracer odd parity multipoles for $t = 1/2$. However, when we consider the cross-power spectrum of two different tracers, these symmetries are broken just like the local relativistic contributions case.

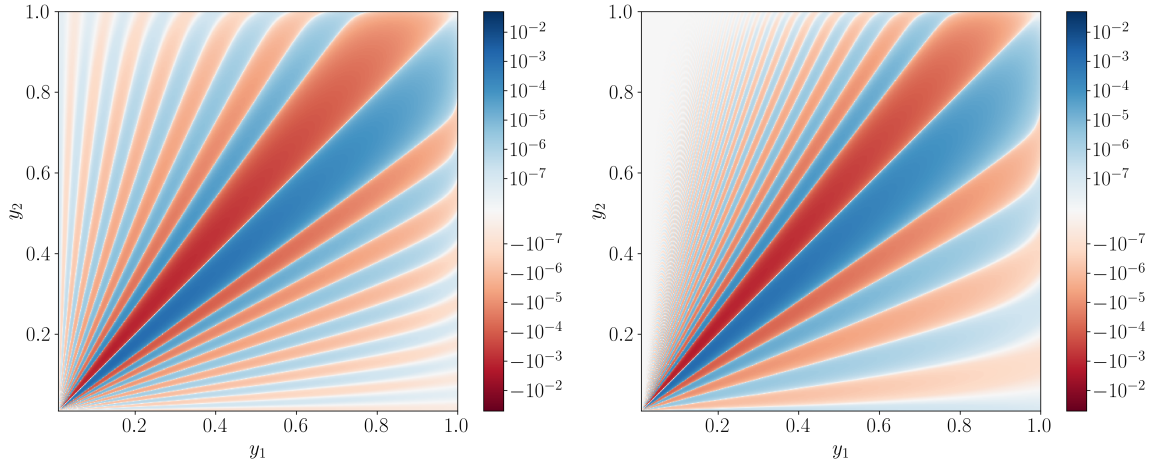


Figure 17: Imaginary single tracer integrand of the dipole for the $I \times I$ contribution with $t = 1/2$ (left) and $t = 0$ (right) for a *Euclid*-like H α survey for $k = 0.01$ at $z = 1.5$. Bottom left corner represents the observer and top right represents the source.

G.1 Convergence and Divergence and Computation Time

For the $I \times S$ (Eq. (C.4)) and $I \times I$ (Eq. (2.20)) contributions, we can do the μ integration analytically, which leaves a single integral over r and a double integral over r_1, r_2 to compute, respectively. To implement this in COSMOWAP Ω , we use Gauss-Legendre quadrature. The convergence of these integrals for different number of Gauss-Legendre nodes, n , is shown in Fig. 18. These integrals converge slower for larger k values, as the frequency of the oscillations in r_1, r_2 increase with k , and therefore, one needs more samples to accurately resolve these oscillations. For our forecasts, we use $n = 256$ as, at that number of nodes, the $I \times I$ term has converged to percentage level at $k = 0.1 h/\text{Mpc}$. Beyond these scales, while the contribution is not as well converged, there is limited impact on our forecasts, and indeed, we have verified that for our forecasts on f_{NL} , the change in constraints and bias from $n = 256$ to $n = 512$ is sub-percentage level.

Here, therefore the computation time for the $I \times I$ term scales as $n^2 n_k$ where n_k is the number of k modes. In the single tracer, for $t = 1/2$, this is halved due to the aforementioned symmetry in the integrand. For the integrated contribution to the covariance, it is however simpler to work with the μ -dependent expressions such that this scales as $n^2 n_k n_\mu$.

We can however compute these integrals more efficiently if we more closely consider the y_1, y_2, k and μ dependences. In particular, in the case where we consider an endpoint LOS we can reduce the amount of required computation for a given analysis. For example, if we consider the $I \times I$ contribution Eq. (2.20) for $t = 0$ (thus $G(y_1, y_2) = y_2$) then it is useful to compute the following integral

$$I_{mn}(p) = \int_0^1 dy_1 e^{i(y_1)p} d\mathcal{Z}_{mn}^I(d, y_1), \quad (\text{G.1})$$

where $\mathcal{Z}_{mn}^I(d, y_1)$ are the coefficients for the given μ and k dependences in an integrated kernel $\mathcal{K}^I(k, \mu, d, r)$

$$\mathcal{K}(k, \mu, d, r) = \sum_n \sum_m k^n \mu^m \mathcal{Z}_{mn}^I(\mu, d, y_1). \quad (\text{G.2})$$

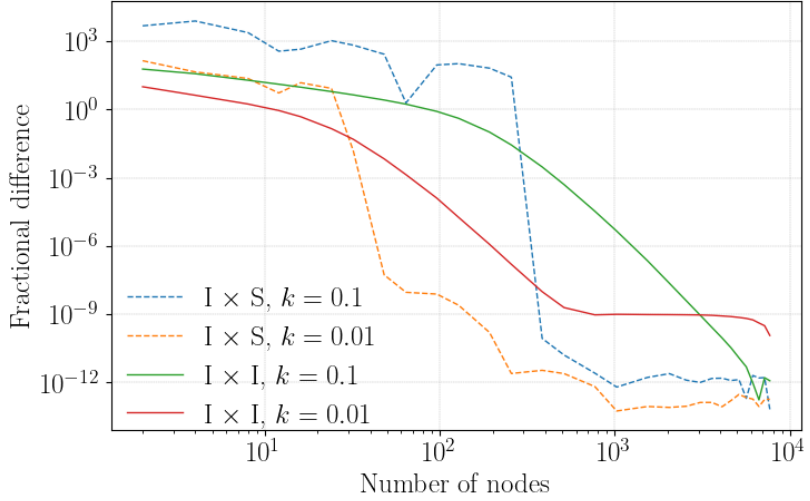


Figure 18: Convergence of the power spectrum monopole ($t = 1/2$) for different numbers of Legendre-Gauss nodes compared to a reference value of $n = 8192$ for two different k -values, plotted for a *Euclid*-like H α survey at $z = 1.5$.

The y_1 integral can be written as

$$\int_0^1 dy_1 e^{iy_1 k \mu d/y_2} d\mathcal{K}(k/y_2, \mu, d, r) = \sum_n \sum_m (k/y_2)^n \mu^m I_{mn}(p) \quad (\text{G.3})$$

where we define $p = k \mu d/y_2$. Interpolating this function there allows us to reduce the dimensions of the integral we need to compute. So therefore the I×I integral involves computing

$$P_{\text{loc}}^{\text{I}\times\text{I}}(k, \mu, d) = e^{-ik\mu d} \sum_n \sum_m \mu^m \int_0^1 dy_2 (k/y_2)^n d y_2^{-3} \mathcal{K}^{\text{I}}(k/y_2, -\mu, d, r_2) \times P(k/y_2) I_{mn}(k\mu/y_2). \quad (\text{G.4})$$

This r_2 integral is quite oscillatory close to the source and therefore we find Filon quadrature to be useful. Note that for Eq. (G.1), we compute this oscillatory integral over a large domain of p and therefore we found fitting the simple y_1 dependence in the kernel coefficients, $\mathcal{Z}_{mn}^{\text{I}}(\mu, d, y_1)$, with a polynomial and then using integration by parts to compute the integral analytically, achieves good results. Similar principles can be implemented for the I×S method. We keep things more flexible by doing the μ integral numerically which allows us to compute the full μ dependent power spectrum once for each redshift bin from which we can trivially obtain the multipoles. This gives $\mathcal{O}(10)$ speed up in computation time compared to the initial analytical μ integration and Gauss-Legendre quadrature, however there is far greater speed up in the computation of the covariances.

H ISW, Time Delay and Lensing Contributions

Fig. 19 and Fig. 20 show the lensing, time delay and ISW contributions separately, for the even and odd contributions to the power spectrum, respectively. Lensing is the dominant integrated effect, particularly at higher redshifts. At smaller redshifts (and particularly for

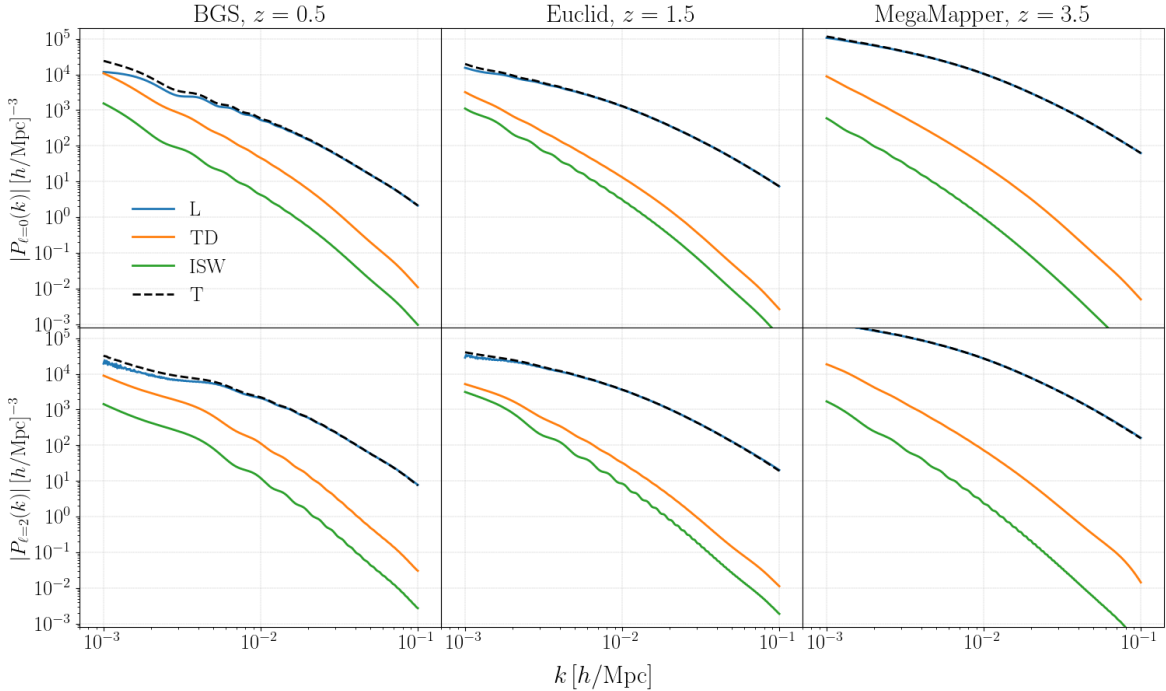


Figure 19: Integrated component contributions of the lensing (L), time delay (TD) and ISW effects to the monopole and quadrupole of the power spectrum. Each contribution contains all the mixing terms with the previous term – e.g. TD contains the mixing terms $\text{TD} \times \text{S}$ and $\text{TD} \times \text{L}$.

the quadrupole), the imaginary part of the lensing kernel, which has a $(d - r)$ dependence, is more important, and this generates the oscillations in the contribution from the sharp cut-off in the Fourier transform at the observer. The time delay and ISW are subdominant to the lensing contribution but are comparatively larger at smaller redshifts and for smaller k – due to their additional $1/q^2$ dependence. The ISW contribution in particular peaks at very low redshifts as it sensitive to the late-time acceleration in expansion.

The cumulative signal-to-noise ratio (SNR) is plotted for each integrated component term for a single-tracer (left) and multi-tracer (right) analysis in Fig. 21. We forecast the lensing term should be detectable for *Euclid*, SKAO2 and MegaMapper in the single-tracer case and indeed, there is limited improvement in the multi-tracer case. However, the effects from time delay and ISW are unlikely to be detectable in the 3D matter power spectrum. Some constraining power is lost on large scales and at low redshifts due to the $k < 2\pi/x(z_{\min})$ cut we impose due to the perturbative wide-separation expansion breaking down.

I Additional Plots

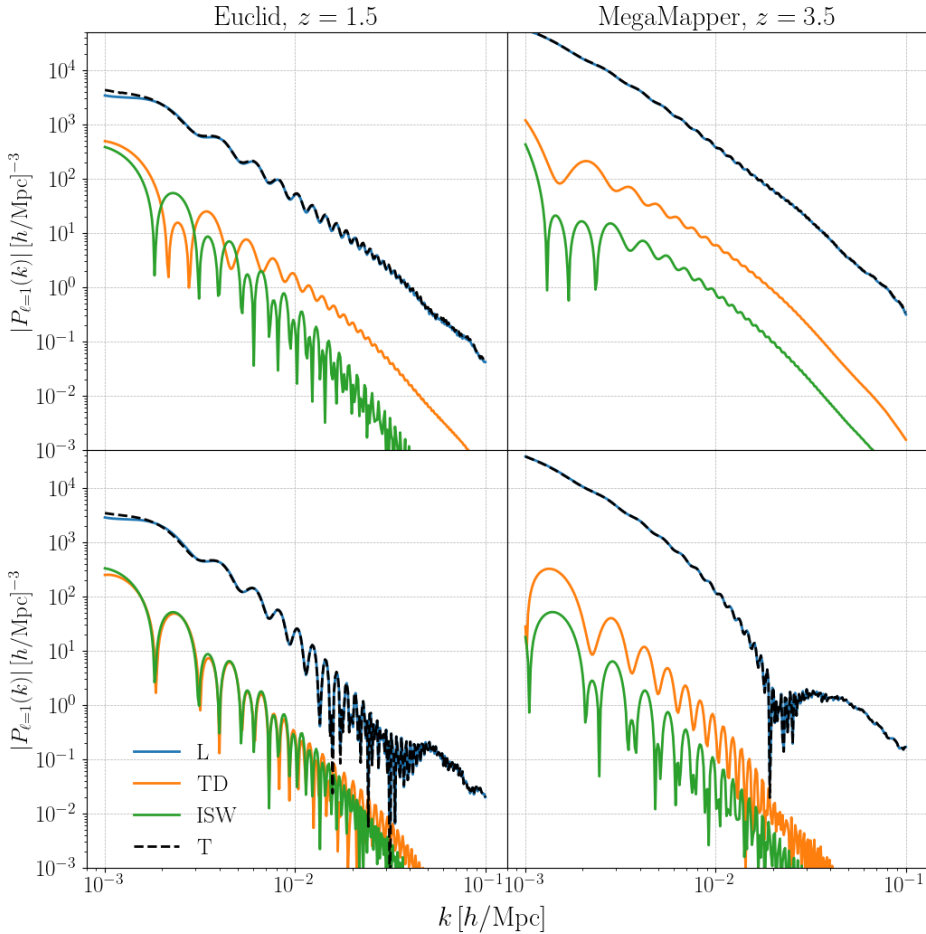


Figure 20: Imaginary integrated component contributions to the dipole of the power spectrum for lensing (L), time delay (TD) and ISW effects for *Euclid* and *MegaMapper*-like surveys, in the single tracer case (bottom panel) and for bright-faint split cross-power spectra (top panel). Each contribution contains all the mixing terms with the previous term – e.g. TD contains the mixing terms TD×S and TD×L.

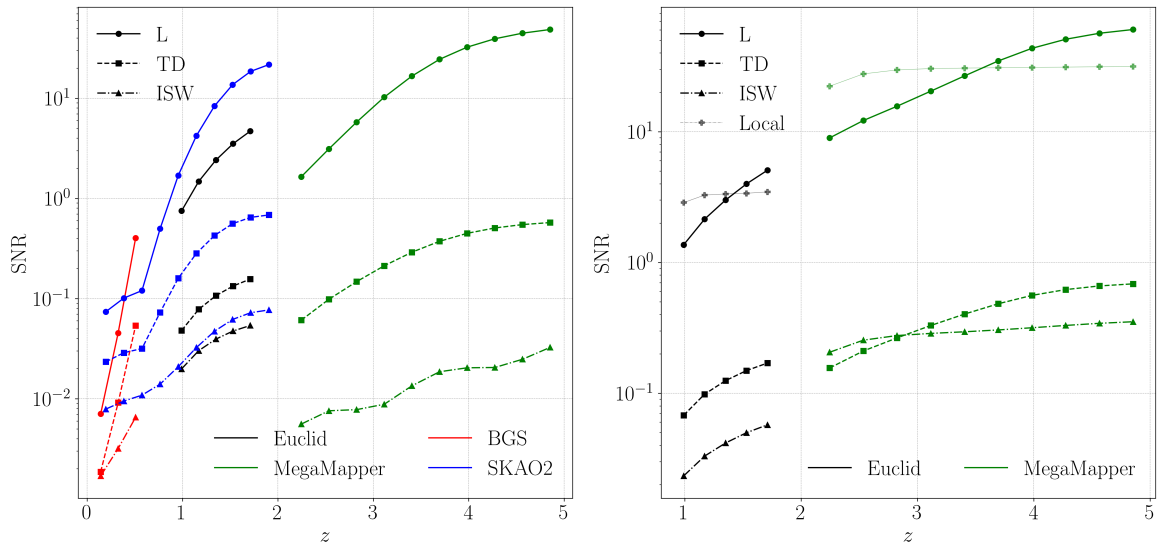


Figure 21: Cumulative SNRs for a single-tracer analysis (left) and a bright-faint split approach (right), for the different integrated terms, plotted over redshift bins. The SNR of the local relativistic term is included for reference in the multi-tracer case. Note that we do not marginalise over any parameters for these SNRs.

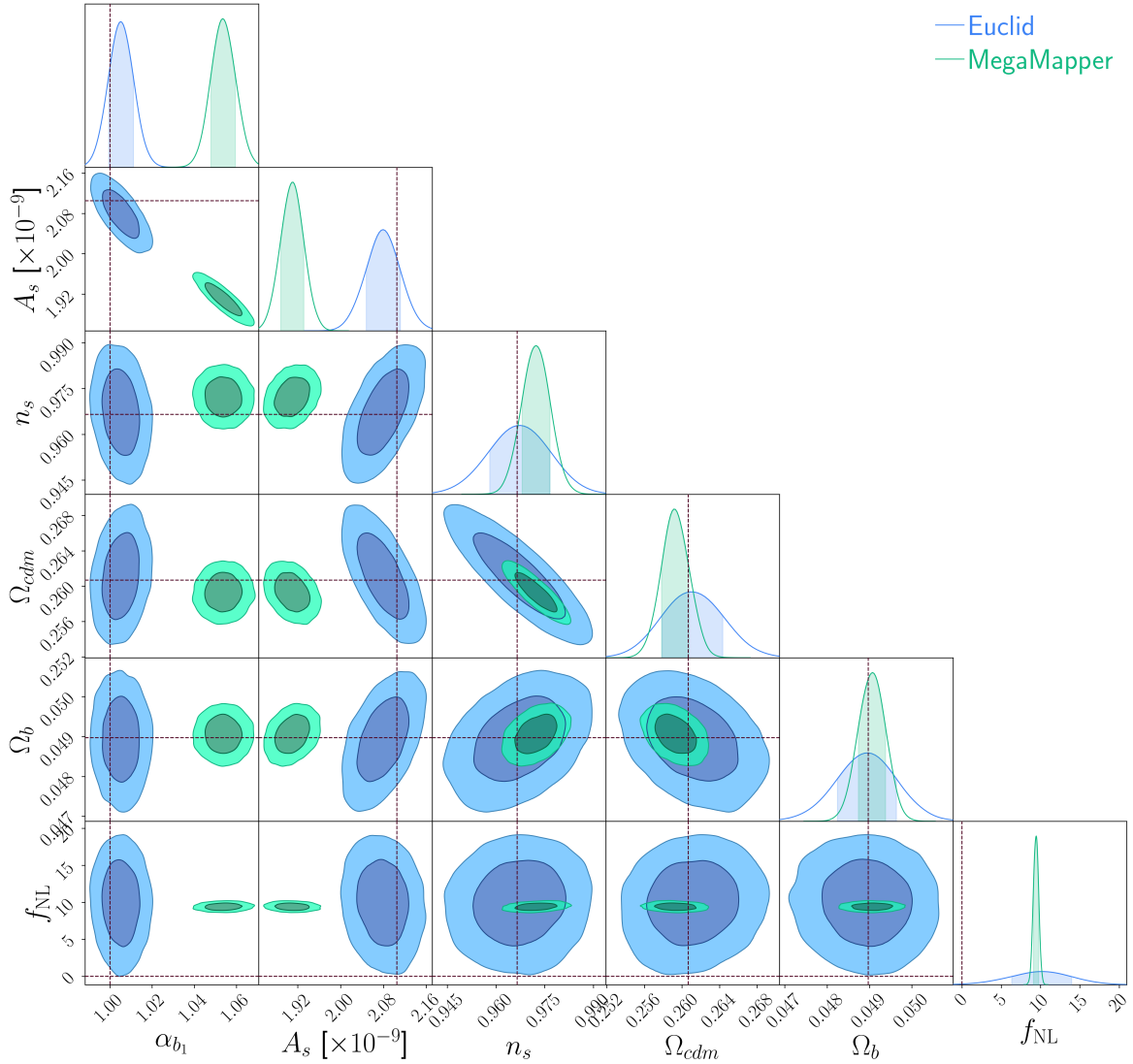


Figure 22: Forecasted marginalised and joint parameter constraints for a *Euclid*-like H α survey (blue) and a MegaMapper-like LBG survey (green), if we neglect integrated, local relativistic and wide-separation effects in our analysis. This is equivalent to Fig. 6 but without the assumption of cosmological priors from *Planck*. Solid colour representing the 1σ constraints and the lighter region denoting the 2σ constraints.

References

- [1] DESI Collaboration, A. Aghamousa, J. Aguilar, S. Ahlen, S. Alam, L.E. Allen et al., *The DESI Experiment Part I: Science, Targeting, and Survey Design*, *arXiv e-prints* (2016) arXiv:1611.00036 [1611.00036].
- [2] Euclid Collaboration, Y. Mellier, Abdurro'uf, J.A. Acevedo Barroso, A. Achúcarro, J. Adamek et al., *Euclid: I. Overview of the Euclid mission*, *A&A* **697** (2025) A1 [2405.13491].
- [3] O. Doré, J. Bock, M. Ashby, P. Capak, A. Cooray, R. de Putter et al., *Cosmology with the SPHEREX All-Sky Spectral Survey*, *arXiv e-prints* (2014) arXiv:1412.4872 [1412.4872].
- [4] D. Spergel, N. Gehrels, J. Breckinridge, M. Donahue, A. Dressler, B.S. Gaudi et al., *Wide-Field InfraRed Survey Telescope-Astrophysics Focused Telescope Assets WFIRST-AFTA Final Report*, *arXiv e-prints* (2013) arXiv:1305.5422 [1305.5422].
- [5] D.J. Schlegel, J.A. Kollmeier, G. Aldering, S. Bailey, C. Baltay, C. Bebek et al., *The MegaMapper: A Stage-5 Spectroscopic Instrument Concept for the Study of Inflation and Dark Energy*, *arXiv e-prints* (2022) arXiv:2209.04322 [2209.04322].
- [6] D.J. Schlegel, S. Ferraro, G. Aldering, C. Baltay, S. BenZvi, R. Besuner et al., *A Spectroscopic Road Map for Cosmic Frontier: DESI, DESI-II, Stage-5*, *arXiv e-prints* (2022) arXiv:2209.03585 [2209.03585].
- [7] A. Achúcarro, M. Biagetti, M. Braglia, G. Cabass, R. Caldwell, E. Castorina et al., *Inflation: Theory and Observations*, *arXiv e-prints* (2022) arXiv:2203.08128 [2203.08128].
- [8] Planck Collaboration, Y. Akrami, F. Arroja, M. Ashdown, J. Aumont, C. Baccigalupi et al., *Planck 2018 results. IX. Constraints on primordial non-Gaussianity*, *A&A* **641** (2020) A9 [1905.05697].
- [9] N. Dalal, O. Doré, D. Huterer and A. Shirokov, *Imprints of primordial non-Gaussianities on large-scale structure: Scale-dependent bias and abundance of virialized objects*, *Phys. Rev. D* **77** (2008) 123514 [0710.4560].
- [10] A. Slosar, C. Hirata, U. Seljak, S. Ho and N. Padmanabhan, *Constraints on local primordial non-Gaussianity from large scale structure*, *J. Cosmology Astropart. Phys.* **2008** (2008) 031 [0805.3580].
- [11] S. Matarrese and L. Verde, *The Effect of Primordial Non-Gaussianity on Halo Bias*, *ApJ* **677** (2008) L77 [0801.4826].
- [12] T. Giannantonio, C. Porciani, J. Carron, A. Amara and A. Pillepich, *Constraining primordial non-Gaussianity with future galaxy surveys*, *MNRAS* **422** (2012) 2854 [1109.0958].
- [13] A. Font-Ribera, P. McDonald, N. Mostek, B.A. Reid, H.-J. Seo and A. Slosar, *DESI and other Dark Energy experiments in the era of neutrino mass measurements*, *J. Cosmology Astropart. Phys.* **2014** (2014) 023 [1308.4164].
- [14] L. Amendola, S. Appleby, A. Avgoustidis, D. Bacon, T. Baker, M. Baldi et al., *Cosmology and fundamental physics with the Euclid satellite*, *Living Reviews in Relativity* **21** (2018) 2 [1606.00180].
- [15] E.-M. Mueller, W.J. Percival and R. Ruggeri, *Optimizing primordial non-Gaussianity measurements from galaxy surveys*, *MNRAS* **485** (2019) 4160 [1702.05088].
- [16] N. Kaiser, *Clustering in real space and in redshift space*, *MNRAS* **227** (1987) 1.
- [17] A.J.S. Hamilton, *Linear Redshift Distortions: a Review*, in *The Evolving Universe*, D. Hamilton, ed., vol. 231 of *Astrophysics and Space Science Library*, p. 185, Jan., 1998, DOI [astro-ph/9708102].
- [18] P. McDonald, *Gravitational redshift and other redshift-space distortions of the imaginary part of the power spectrum*, *J. Cosmology Astropart. Phys.* **2009** (2009) 026 [0907.5220].

- [19] J. Yoo, *General relativistic description of the observed galaxy power spectrum: Do we understand what we measure?*, *Phys. Rev. D* **82** (2010) 083508 [[1009.3021](#)].
- [20] C. Bonvin and R. Durrer, *What galaxy surveys really measure*, *Phys. Rev. D* **84** (2011) 063505 [[1105.5280](#)].
- [21] A. Challinor and A. Lewis, *Linear power spectrum of observed source number counts*, *Phys. Rev. D* **84** (2011) 043516 [[1105.5292](#)].
- [22] M. Bruni, R. Crittenden, K. Koyama, R. Maartens, C. Pitrou and D. Wands, *Disentangling non-Gaussianity, bias, and general relativistic effects in the galaxy distribution*, *Phys. Rev. D* **85** (2012) 041301 [[1106.3999](#)].
- [23] S. Camera, R. Maartens and M.G. Santos, *Einstein’s legacy in galaxy surveys.*, *MNRAS* **451** (2015) L80 [[1412.4781](#)].
- [24] D. Alonso, P. Bull, P.G. Ferreira, R. Maartens and M.G. Santos, *Ultra-large-scale Cosmology in Next-generation Experiments with Single Tracers*, *ApJ* **814** (2015) 145 [[1505.07596](#)].
- [25] D. Alonso and P.G. Ferreira, *Constraining ultralarge-scale cosmology with multiple tracers in optical and radio surveys*, *Phys. Rev. D* **92** (2015) 063525 [[1507.03550](#)].
- [26] J.-A. Viljoen, J. Fonseca and R. Maartens, *Multi-wavelength spectroscopic probes: biases from neglecting light-cone effects*, *J. Cosmology Astropart. Phys.* **2021** (2021) 004 [[2108.05746](#)].
- [27] D. Jeong, F. Schmidt and C.M. Hirata, *Large-scale clustering of galaxies in general relativity*, *Phys. Rev. D* **85** (2012) 023504 [[1107.5427](#)].
- [28] M.S. Wang, F. Beutler and D. Bacon, *Impact of relativistic effects on the primordial non-Gaussianity signature in the large-scale clustering of quasars*, *MNRAS* **499** (2020) 2598 [[2007.01802](#)].
- [29] M. Foglieni, M. Pantiri, E. Di Dio and E. Castorina, *Large Scale Limit of the Observed Galaxy Power Spectrum*, *Phys. Rev. Lett.* **131** (2023) 111201 [[2303.03142](#)].
- [30] S. Jolicoeur, S.L. Guedezounme, R. Maartens, P. Paul, C. Clarkson and S. Camera, *Relativistic and wide-angle corrections to galaxy power spectra*, *JCAP* **08** (2024) 027 [[2406.06274](#)].
- [31] S.L. Guedezounme, S. Jolicoeur and R. Maartens, *Primordial non-Gaussianity — the effects of relativistic and wide-angle corrections to the power spectrum*, *JCAP* **07** (2025) 063 [[2412.06553](#)].
- [32] R. Maartens, J. Fonseca, S. Camera, S. Jolicoeur, J.-A. Viljoen and C. Clarkson, *Magnification and evolution biases in large-scale structure surveys*, *J. Cosmology Astropart. Phys.* **2021** (2021) 009 [[2107.13401](#)].
- [33] L. Lombriser, J. Yoo and K. Koyama, *Relativistic effects in galaxy clustering in a parametrized post-Friedmann universe*, *Phys. Rev. D* **87** (2013) 104019 [[1301.3132](#)].
- [34] C. Bonvin, F. Oliveira Franco and P. Fleury, *A null test of the equivalence principle using relativistic effects in galaxy surveys*, *J. Cosmology Astropart. Phys.* **2020** (2020) 004 [[2004.06457](#)].
- [35] S. Castello, N. Grimm and C. Bonvin, *Rescuing constraints on modified gravity using gravitational redshift in large-scale structure*, *Phys. Rev. D* **106** (2022) 083511 [[2204.11507](#)].
- [36] D. Sobral Blanco and C. Bonvin, *Measuring the distortion of time with relativistic effects in large-scale structure*, *MNRAS* **519** (2023) L39 [[2205.02567](#)].
- [37] S. Castello, Z. Zheng, C. Bonvin and L. Amendola, *Testing the equivalence principle across the Universe: A model-independent approach with galaxy multitracing*, *Phys. Rev. D* **111** (2025) 123559 [[2412.08627](#)].

- [38] C. Bonvin, *Isolating relativistic effects in large-scale structure*, *Classical and Quantum Gravity* **31** (2014) 234002 [[1409.2224](#)].
- [39] C. Bonvin, L. Hui and E. Gaztañaga, *Asymmetric galaxy correlation functions*, *Phys. Rev. D* **89** (2014) 083535 [[1309.1321](#)].
- [40] C. Bonvin, L. Hui and E. Gaztanaga, *Optimising the measurement of relativistic distortions in large-scale structure*, *J. Cosmology Astropart. Phys.* **2016** (2016) 021 [[1512.03566](#)].
- [41] E. Gaztanaga, C. Bonvin and L. Hui, *Measurement of the dipole in the cross-correlation function of galaxies*, *J. Cosmology Astropart. Phys.* **2017** (2017) 032 [[1512.03918](#)].
- [42] F. Montano and S. Camera, *Detecting relativistic Doppler in galaxy clustering with tailored galaxy samples*, *Physics of the Dark Universe* **46** (2024) 101570 [[2309.12400](#)].
- [43] F. Montano and S. Camera, *Detecting relativistic Doppler by multi-tracing a single galaxy population*, *Physics of the Dark Universe* **46** (2024) 101634 [[2407.06284](#)].
- [44] M. Novara, F. Montano and S. Camera, *Detecting local and integrated relativistic effects by multi-tracing a single galaxy population in harmonic space*, *Physics of the Dark Universe* **50** (2025) 102160.
- [45] U. Seljak, *Extracting Primordial Non-Gaussianity without Cosmic Variance*, *Phys. Rev. Lett.* **102** (2009) 021302 [[0807.1770](#)].
- [46] A. Barreira and E. Krause, *Towards optimal and robust f_{NL} constraints with multi-tracer analyses*, *J. Cosmology Astropart. Phys.* **2023** (2023) 044 [[2302.09066](#)].
- [47] D. Karagiannis, R. Maartens, J. Fonseca, S. Camera and C. Clarkson, *Multi-tracer power spectra and bispectra: formalism*, *J. Cosmology Astropart. Phys.* **2024** (2024) 034 [[2305.04028](#)].
- [48] V. Tansella, C. Bonvin, R. Durrer, B. Ghosh and E. Sellentin, *The full-sky relativistic correlation function and power spectrum of galaxy number counts. Part I: theoretical aspects*, *J. Cosmology Astropart. Phys.* **2018** (2018) 019 [[1708.00492](#)].
- [49] E. Castorina and E. Di Dio, *The observed galaxy power spectrum in General Relativity*, *J. Cosmology Astropart. Phys.* **2022** (2022) 061 [[2106.08857](#)].
- [50] D.N. Limber, *The Analysis of Counts of the Extragalactic Nebulae in Terms of a Fluctuating Density Field.*, *ApJ* **117** (1953) 134.
- [51] M. Noorikuhani and R. Scoccimarro, *Wide-angle and relativistic effects in Fourier-space clustering statistics*, *Phys. Rev. D* **107** (2023) 083528 [[2207.12383](#)].
- [52] K. Yamamoto, M. Nakamichi, A. Kamino, B.A. Bassett and H. Nishioka, *A Measurement of the Quadrupole Power Spectrum in the Clustering of the 2dF QSO Survey*, *PASJ* **58** (2006) 93 [[astro-ph/0505115](#)].
- [53] F. Beutler, S. Saito, H.-J. Seo, J. Brinkmann, K.S. Dawson, D.J. Eisenstein et al., *The clustering of galaxies in the SDSS-III Baryon Oscillation Spectroscopic Survey: testing gravity with redshift space distortions using the power spectrum multipoles*, *MNRAS* **443** (2014) 1065 [[1312.4611](#)].
- [54] D. Bianchi, H. Gil-Marín, R. Ruggeri and W.J. Percival, *Measuring line-of-sight-dependent Fourier-space clustering using FFTs*, *MNRAS* **453** (2015) L11 [[1505.05341](#)].
- [55] R. Scoccimarro, *Fast estimators for redshift-space clustering*, *Phys. Rev. D* **92** (2015) 083532 [[1506.02729](#)].
- [56] S. Zaroubi and Y. Hoffman, *Clustering in Redshift Space: Linear Theory*, *ApJ* **462** (1996) 25.
- [57] E. Castorina and M. White, *Beyond the plane-parallel approximation for redshift surveys*, *MNRAS* **476** (2018) 4403 [[1709.09730](#)].

- [58] C. Addis, C. Guandalin and C. Clarkson, *Multipoles of the galaxy bispectrum on a light cone: wide-separation and relativistic corrections*, *J. Cosmology Astropart. Phys.* **2025** (2025) 080 [[2407.00168](#)].
- [59] P. Reimberg, F. Bernardeau and C. Pitrou, *Redshift-space distortions with wide angular separations*, *J. Cosmology Astropart. Phys.* **2016** (2016) 048 [[1506.06596](#)].
- [60] F. Beutler and E. Di Dio, *Modeling relativistic contributions to the halo power spectrum dipole*, *J. Cosmology Astropart. Phys.* **2020** (2020) 048 [[2004.08014](#)].
- [61] P. Paul, C. Clarkson and R. Maartens, *Wide-angle effects in multi-tracer power spectra with Doppler corrections*, *JCAP* **04** (2023) 067 [[2208.04819](#)].
- [62] J.N. Benabou, I. Sands, H.S. Grasshorn Gebhardt, C. Heinrich and O. Doré, *Wide-Angle Effects in the Power Spectrum Multipoles in Next-Generation Redshift Surveys*, *arXiv e-prints* (2024) arXiv:2404.04811 [[2404.04811](#)].
- [63] R.Y. Wen, H.S.G. Gebhardt, C. Heinrich and O. Doré, *Linear relativistic corrections in the spherical Fourier-Bessel power spectrum*, *Phys. Rev. D* **110** (2024) 123501 [[2407.02753](#)].
- [64] F. Semenzato, D. Bertacca and A. Raccanelli, *Full-sky spherical Fourier-Bessel power spectrum in general relativity*, *Phys. Rev. D* **111** (2025) 023522 [[2406.09545](#)].
- [65] C. Addis, “CosmoWAP: Power spectra and bispectra analyzer.” Astrophysics Source Code Library, record ascl:2507.020, July, 2025.
- [66] C. Addis, “MathWAP: Compute power spectra bispectra contributions from perturbation theory.” Astrophysics Source Code Library, record ascl:2507.019, July, 2025.
- [67] H.A. Feldman, N. Kaiser and J.A. Peacock, *Power-Spectrum Analysis of Three-dimensional Redshift Surveys*, *ApJ* **426** (1994) 23 [[astro-ph/9304022](#)].
- [68] M.J. Wilson, J.A. Peacock, A.N. Taylor and S. de la Torre, *Rapid modelling of the redshift-space power spectrum multipoles for a masked density field*, *MNRAS* **464** (2017) 3121 [[1511.07799](#)].
- [69] Planck Collaboration, N. Aghanim, Y. Akrami, M. Ashdown, J. Aumont, C. Baccigalupi et al., *Planck 2018 results. VI. Cosmological parameters*, *A&A* **641** (2020) A6 [[1807.06209](#)].
- [70] D.S. Blanco, C. Bonvin, C. Clarkson and R. Maartens, *Using relativistic effects in large-scale structure to constrain astrophysical properties of galaxy populations*, *J. Cosmology Astropart. Phys.* **2024** (2024) 029 [[2406.19908](#)].
- [71] A. Barreira, G. Cabass, F. Schmidt, A. Pillepich and D. Nelson, *Galaxy bias and primordial non-Gaussianity: insights from galaxy formation simulations with IllustrisTNG*, *J. Cosmology Astropart. Phys.* **2020** (2020) 013 [[2006.09368](#)].
- [72] A. Barreira, *Predictions for local PNG bias in the galaxy power spectrum and bispectrum and the consequences for f_{NL} constraints*, *J. Cosmology Astropart. Phys.* **2022** (2022) 033 [[2107.06887](#)].
- [73] A. Gutiérrez Adame, S. Avila, V. Gonzalez-Perez, G. Yepes, M. Pellejero, M.S. Wang et al., *PNG-UNITsims: Halo clustering response to primordial non-Gaussianities as a function of mass*, *A&A* **689** (2024) A69 [[2312.12405](#)].
- [74] E. Fondi, L. Verde, F. Villaescusa-Navarro, M. Baldi, W.R. Coulton, G. Jung et al., *Taming assembly bias for primordial non-Gaussianity*, *J. Cosmology Astropart. Phys.* **2024** (2024) 048 [[2311.10088](#)].
- [75] A. Barreira, *Can we actually constrain f_{NL} using the scale-dependent bias effect? An illustration of the impact of galaxy bias uncertainties using the BOSS DR12 galaxy power spectrum*, *J. Cosmology Astropart. Phys.* **2022** (2022) 013 [[2205.05673](#)].

- [76] M. Tellarini, A.J. Ross, G. Tasinato and D. Wands, *Galaxy bispectrum, primordial non-Gaussianity and redshift space distortions*, *J. Cosmology Astropart. Phys.* **2016** (2016) 014 [[1603.06814](#)].
- [77] T.D. Kitching, A. Amara, F.B. Abdalla, B. Joachimi and A. Refregier, *Cosmological systematics beyond nuisance parameters: form-filling functions*, *MNRAS* **399** (2009) 2107 [[0812.1966](#)].
- [78] A. Lewis and S. Bridle, *Cosmological parameters from CMB and other data: A Monte Carlo approach*, *Phys. Rev. D* **66** (2002) 103511 [[astro-ph/0205436](#)].
- [79] A. Lewis, *Efficient sampling of fast and slow cosmological parameters*, *Phys. Rev. D* **87** (2013) 103529 [[1304.4473](#)].
- [80] J. Torrado and A. Lewis, *Cobaya: code for Bayesian analysis of hierarchical physical models*, *J. Cosmology Astropart. Phys.* **2021** (2021) 057 [[2005.05290](#)].
- [81] A. Spurio Mancini, D. Piras, J. Alsing, B. Joachimi and M.P. Hobson, *COSMOPOWER: emulating cosmological power spectra for accelerated Bayesian inference from next-generation surveys*, *MNRAS* **511** (2022) 1771 [[2106.03846](#)].
- [82] A.J. Mead, S. Brieden, T. Tröster and C. Heymans, *HMCODE-2020: improved modelling of non-linear cosmological power spectra with baryonic feedback*, *MNRAS* **502** (2021) 1401 [[2009.01858](#)].
- [83] A.G. Kim, E.V. Linder, R. Miquel and N. Mostek, *Effects of systematic uncertainties on the supernova determination of cosmological parameters*, *MNRAS* **347** (2004) 909 [[astro-ph/0304509](#)].
- [84] A.N. Taylor, T.D. Kitching, D.J. Bacon and A.F. Heavens, *Probing dark energy with the shear-ratio geometric test*, *MNRAS* **374** (2007) 1377 [[astro-ph/0606416](#)].
- [85] J.L. Bernal, N. Bellomo, A. Raccaelli and L. Verde, *Beware of commonly used approximations. Part II. Estimating systematic biases in the best-fit parameters*, *J. Cosmology Astropart. Phys.* **2020** (2020) 017 [[2005.09666](#)].
- [86] J. Lesgourgues, *The Cosmic Linear Anisotropy Solving System (CLASS) I: Overview*, *arXiv e-prints* (2011) arXiv:1104.2932 [[1104.2932](#)].
- [87] D. Blas, J. Lesgourgues and T. Tram, *The cosmic linear anisotropy solving system (class). part ii: Approximation schemes*, *Journal of Cosmology and Astroparticle Physics* **2011** (2011) 034–034.
- [88] C.R. Harris, K.J. Millman, S.J. van der Walt, R. Gommers, P. Virtanen, D. Cournapeau et al., *Array programming with NumPy*, *Nature* **585** (2020) 357 [[2006.10256](#)].
- [89] P. Virtanen, R. Gommers, T.E. Oliphant, M. Haberland, T. Reddy, D. Cournapeau et al., *SciPy 1.0: fundamental algorithms for scientific computing in Python*, *Nature Methods* **17** (2020) 261 [[1907.10121](#)].
- [90] J.D. Hunter, *Matplotlib: A 2D Graphics Environment*, *Computing in Science and Engineering* **9** (2007) 90.
- [91] S.R. Hinton, *ChainConsumer*, *The Journal of Open Source Software* **1** (2016) 00045.
- [92] L. Pozzetti, C.M. Hirata, J.E. Geach, A. Cimatti, C. Baugh, O. Cucciati et al., *Modelling the number density of H α emitters for future spectroscopic near-IR space missions*, *A&A* **590** (2016) A3 [[1603.01453](#)].
- [93] Euclid Collaboration, A. Blanchard, S. Camera, C. Carbone, V.F. Cardone, S. Casas et al., *Euclid preparation. VII. Forecast validation for Euclid cosmological probes*, *A&A* **642** (2020) A191 [[1910.09273](#)].

- [94] H. Pan, D. Obreschkow, C. Howlett, C.d.P. Lagos, P.J. Elahi, C. Baugh et al., *Multiwavelength consensus of large-scale linear bias*, *MNRAS* **493** (2020) 747 [[1909.12069](#)].
- [95] S. Cole, C.G. Lacey, C.M. Baugh and C.S. Frenk, *Hierarchical galaxy formation*, *MNRAS* **319** (2000) 168 [[astro-ph/0007281](#)].
- [96] V. Gonzalez-Perez, J. Comparat, P. Norberg, C.M. Baugh, S. Contreras, C. Lacey et al., *The host dark matter haloes of [O II] emitters at $0.5 < z < 1.5$* , *MNRAS* **474** (2018) 4024 [[1708.07628](#)].
- [97] M.J. Wilson and M. White, *Cosmology with dropout selection: straw-man surveys & CMB lensing*, *J. Cosmology Astropart. Phys.* **2019** (2019) 015 [[1904.13378](#)].
- [98] P. Schechter, *An analytic expression for the luminosity function for galaxies.*, *ApJ* **203** (1976) 297.
- [99] Y. Ono, M. Ouchi, Y. Harikane, J. Toshikawa, M. Rauch, S. Yuma et al., *Great Optically Luminous Dropout Research Using Subaru HSC (GOLDRUSH). I. UV luminosity functions at $z \sim 4\text{-}7$ derived with the half-million dropouts on the 100 deg 2 sky*, *PASJ* **70** (2018) S10 [[1704.06004](#)].
- [100] J. Loveday, P. Norberg, I.K. Baldry, S.P. Driver, A.M. Hopkins, J.A. Peacock et al., *Galaxy and Mass Assembly (GAMA): ugriz galaxy luminosity functions*, *MNRAS* **420** (2012) 1239 [[1111.0166](#)].
- [101] G. Jelic-Cizmek, F. Lepori, C. Bonvin and R. Durrer, *On the importance of lensing for galaxy clustering in photometric and spectroscopic surveys*, *J. Cosmology Astropart. Phys.* **2021** (2021) 055 [[2004.12981](#)].
- [102] S. Yahya, P. Bull, M.G. Santos, M. Silva, R. Maartens, P. Okouma et al., *Cosmological performance of SKA H I galaxy surveys*, *MNRAS* **450** (2015) 2251 [[1412.4700](#)].
- [103] P. Bull, *Extending Cosmological Tests of General Relativity with the Square Kilometre Array*, *ApJ* **817** (2016) 26 [[1509.07562](#)].
- [104] L.D. Ferramacho, M.G. Santos, M.J. Jarvis and S. Camera, *Radio galaxy populations and the multitracer technique: pushing the limits on primordial non-Gaussianity*, *MNRAS* **442** (2014) 2511 [[1402.2290](#)].
- [105] C. Bonvin, F. Lepori, S. Schulz, I. Tutusaus, J. Adamek and P. Fosalba, *A case study for measuring the relativistic dipole of a galaxy cross-correlation with the Dark Energy Spectroscopic Instrument*, *MNRAS* **525** (2023) 4611 [[2306.04213](#)].
- [106] A.J.S. Hamilton, C.D. Rimes and R. Scoccimarro, *On measuring the covariance matrix of the non-linear power spectrum from simulations*, *MNRAS* **371** (2006) 1188 [[astro-ph/0511416](#)].
- [107] M.-A. Breton, Y. Rasera, A. Taruya, O. Lacombe and S. Saga, *Imprints of relativistic effects on the asymmetry of the halo cross-correlation function: from linear to non-linear scales*, *MNRAS* **483** (2019) 2671 [[1803.04294](#)].
- [108] J. Adamek, D. Daverio, R. Durrer and M. Kunz, *gevolution: a cosmological N-body code based on General Relativity*, *J. Cosmology Astropart. Phys.* **2016** (2016) 053 [[1604.06065](#)].
- [109] R. Scoccimarro, M. Zaldarriaga and L. Hui, *Power Spectrum Correlations Induced by Nonlinear Clustering*, *ApJ* **527** (1999) 1 [[astro-ph/9901099](#)].
- [110] K.C. Chan and L. Blot, *Assessment of the Information Content of the Power Spectrum and Bispectrum*, *arXiv e-prints* (2016) arXiv:1610.06585 [[1610.06585](#)].
- [111] D. Wadekar and R. Scoccimarro, *Galaxy power spectrum multipoles covariance in perturbation theory*, *Phys. Rev. D* **102** (2020) 123517 [[1910.02914](#)].
- [112] R.E. Smith, *Covariance of cross-correlations: towards efficient measures for large-scale structure*, *MNRAS* **400** (2009) 851 [[0810.1960](#)].